LAVA FLOW HAZARD PREDICTION AND MONITORING WITH UNMANNED AERIAL SYSTEMS: CASE STUDIES FROM THE 2014-2015 PĀHOA LAVA FLOW CRISIS, HAWAIʻI

A THESIS SUBMITTED TO THE GRADUATE DIVISION OF THE UNIVERSITY

OF HAWAIʻI AT MĀNOA IN PARTIAL FULFILMENT OF THE REQUIREMENTS

FOR THE DEGREE OF

MASTER OF SCIENCE

IN

GEOLOGY AND GEOPHYSICS

MAY 2018

By

Nicolas R. Turner

Thesis Committee:

Bruce Houghton, Chairperson

Scott Rowland

Pete Mouginis-Mark

Keyword: pāhoehoe, unmanned aerial systems, lava flow, hazards

Acknowledgements

I thank my advisor Bruce Houghton for his support and guidance during my time at UH Mānoa. For the amazing field work I was fortunate to experience including trips to Stromboli, Italy and his home country of New Zealand. To my committee members and great teachers Scott Rowland and Pete Mouginis-Mark for their helpful comments and review of my thesis. I am grateful for financial support from the National Science Foundation GRFP and the National Disaster Preparedness Training Center.

During the Pāhoa lava flow crisis when the data from these studies were collected, I was employed at the Spatial Data Analysis and Visualization lab (SDAV) at the University of Hawai‘i at Hilo. This research would not have been possible without the incredible support from Ryan Perroy who also reviewed my successful NSF GRFP proposal days before the deadline. Nathan Stephenson and Arthur Cunningham for their hard work and countless hours in the field with me. Don Straney for providing funding for my position at SDAV during my last year at UH Hilo. Darryl Oliveira and the great staff at Hawaii County Civil Defense that granted us permission to access the June 27th flow and coordinated with landowners. Asia Wasser for her amazing help in coordinating and sharing critical datasets during the crisis. Collaborators from the Hawaiian Volcano Observatory, especially Tim Orr and Matt Patrick who always seemed to be in the field and provided helpful insights into the latest flow activity. Ken Hon for his helpful advice and detailed insights into pāhoehoe behavior and to his Geology students for their help in the field. To my fiancée Josephine Sanchez for her unwavering support and allowing me to use our home as an early morning staging area before field missions.

Finally, this thesis is dedicated to the people of Pāhoa and surrounding communities. As an Ainaloa resident, I called the Puna district home for six years. The June 27th flow while not physically destructive, still had a significant impact on our community. The motivation for this work was to improve our ability to monitor and better predict the behavior of pāhoehoe flows to help reduce some of the uncertainty that pained Puna communities during the crisis.

Abstract

During the 2014–2015 Pāhoa lava flow crisis on the island of Hawai‘i, we used a low-altitude unmanned aerial system (UAS) to quickly and repeatedly image the active front of a slowly advancing pāhoehoe lava flow dubbed the June 27th flow. This imagery was used to generate a series of 1 m spatial resolution bare-earth digital elevation models (DEMs) and associated paths of steepest descent over the study area. Our updated DEM models show that future flows in this area will likely be deflected by these 2014-2015 flows, possibly threatening communities not directly impacted by the original 2014–2015 lava flow. Over a 4-week period, a series of very high spatial resolution orthomosaics (0.05 m) and digital elevation models (DEM) (0.3 m) provided new insights into the processes that control flow inflation, lava tube growth, flow-front supply rates and subsequent breakouts. Repeated measurements of volume showed a cumulative increase by 1.9 million m^3, new supply that was partitioned between inflation (56.5%), surface breakouts (1.4%) and lateral breakouts (42.1%). Detailed measurements of stress cracks and overall growth rates define precursors to locate surge-triggered breakouts. This study provides the first use of UAS to measure the combination of inflation, volume, eruption rate, and morphological changes from high spatial resolution imagery of an evolving flow front, parameters that are all critical to improving our understanding of pāhoehoe behavior in both a hazards context and fundamental flow processes. We demonstrate the value of deploying UAS during a dynamically evolving volcanic crisis and suggest that this technology can fill critical monitoring gaps for Kīlauea and other active volcanoes worldwide.

Table of Contents

Chapter 1 1

Chapter 2 4

2.1 Introduction 4

2.1.1 Lava flow monitoring techniques 5

2.1.2 The 2014–2015 Pāhoa lava flow crisis 5

2.2 Methods 6

2.2.1 UAS flight operations 6

2.2.2 Data analysis and processing 8

2.3 Results 12

2.4 Discussion 15

2.4.1 Implications for lava flow monitoring 15

2.4.2 Applications for other lava flow models 17

2.4.3 Successful volcano monitoring with UAS 19

2.4.4 Additional applications for UAS in lava flow monitoring 20

2.5.1 Conclusions 20

Chapter 3 22

3.1 Introduction 22

3.1.1 Processes of flow advancement and implications for hazard management 22

3.1.2 Background 23

3.1.3 The current eruption 23

3.1.4 The June 27th lava flow 23

3.2 Methods 25

3.2.1 UAS flight operations 25

3.2.2 Data processing workflow 26

3.3 Results 27

3.3.1 General findings 27

3.3.2 Rise of a tumulus 30

3.3.3 Tube geometry 32

3.3.4 Active inflation in the study region 36

3.4 Discussion 38

3.4.1 Implications for active lava tube development 38

3.4.2 Summit DI events and influence on flow activity 39

3.4.3 Potential precursors to breakouts 40

3.5 Conclusions 41

Chapter 4 48

Final Conclusions 48

4.1 The role of unmanned aerial systems in volcanology 48

4.2 Research limitations 49

4.2.1 Chapter 2 49

4.2.2 Chapter 3 50

4.3 Future Research **50**
4.3.1 Additional Sensor Payloads **50**
4.3.2 Swarm Mapping **51**
4.3.3 Machine Learning Applications **51**
4.3.4 Remote Drone Ports **52**
4.3.5 UAS Platforms **52**

References **54**

List of Tables

Table 1 Chapter 2 Table of GCPs used per flight segment. 41
Table 2 Chapter 3 table of crack measurements along sinuous tumulus. 43

List of Figures

Figure 2.1 Map of project study site and GCPs..... 7
Figure 2.2 Imagery processing workflow. 9
Figure 2.3 Paths of steepest descent comparison. 13
Figure 2.4 Optimal DEM resolution assessment. 14
Figure 2.5 UAS and GPS DEM quality assessment. 14
Figure 2.6 Comparison of hazard potential with updated topography. 18
Figure 3.1 Map of study site showing key landmarks. 25
Figure 3.2 Map of key morphological features within study site. 25
Figure 3.3 Plot showing volume of lava supply over time.....28
Figure 3.4 Comparison of UAS DEM to ground-based surveys. 31
Figure 3.5 Time-series figure showing surge-triggered breakouts. 35
Figure 3.6 Time-series data showing digital transects of inflation across the flow front. 36
Figure 3.7 Time-series data showing inflation hotspots across the flow field. 37

Chapter 1

Introduction

Thesis Overview

Kīlauea is one of the world's most active volcanoes with the ongoing Puʻu ʻŌʻō eruption spanning 35 years of eruptive activity (as of this writing April, 2018). Since the eruption began in 1983, it has been the longest East Rift Zone eruption in more than 500 years (Orr et al. 2013). Volcanism at Kīlauea predominantly produces lava effusion in the form of 'a'ā and pāhoehoe flows. Pāhoehoe flows in particular form insulated tube systems that can carry fresh lava many kilometers away from the source vent and sometimes pose a direct hazard to nearby communities on the Island of Hawaiʻi. This thesis investigates the integration of emerging technology from the fields of robotics, computer vision, and remote sensing to accurately quantify the physical processes of pahoehoe flow-front evolution and advance.

Pāhoehoe lava flows pose major threats to communities living near active basaltic volcanoes worldwide (Hamilton et al. 2013; Del Negro et al. 2016). Estimating lava flow hazards is important prior to eruptions for regional planning purposes, but becomes critical during times of heightened eruption activity (Gonzalez et al. 2015; Poland et al. 2016; Jenkins et al. 2017). Pāhoehoe lava flows generally advance slower than ʻaʻā flows; however, they can travel equal or even greater distances and spread out over larger areas, posing a more significant long-term threat (Self et al. 1998).

The behavior of an advancing flow is influenced by external and internal factors. External factors include slope gradient, surface roughness, and other topographic and landscape features, while internal factors include variations in lava supply, viscosity, yield strength, rates of inflation, and the geometry of the feeder channels or tube system (Mattox et al. 1993; Kauahikaua et al. 1998; Hon et al. 2003). Over days or weeks, new lobes can break out from the flow front or along margins farther up-slope, while older lobes can become barriers, deflecting younger flows and altering the original topography (Walker et al. 1991; Hon et al. 1994; Anderson et al. 2012).

Pāhoehoe flows exhibit complex and irregular emplacement dynamics, morphologies, and growth processes across multiple spatial scales. To accurately quantify this variety of

spatial patterns requires methods that can capture both the scale of the flow and the critical details simultaneously. Ground-based surveys for lava flow monitoring rely on GPS, lidar, thermal imagery and field photogrammetry (including Structure-from-Motion based techniques) to capture three-dimensional data, but have trouble scaling between toe-sized and large-scale flow dynamics. These limitations make ground-based approaches ideal for studying isolated features of a flow, but they are not suited to capture processes across the entire flow field (Cashman et al. 2013; Hamilton et al. 2013). Satellite-based observations are widely used for lava flow monitoring and offer large spatial coverage during an eruption. However, frequent cloud coverage, coarse spatial resolution, and long re-acquisition intervals all present problems for these platforms to monitor active lava flows. Manned aircraft provide higher spatial resolution imagery, but are expensive to operate, struggle to provide consistent data (compared to automated UAS flights), and are often restricted to higher altitudes.

Advancements in the manufacturing of electronics has brought prices down for miniturized electronic sensors in large part due to the explosion of growth in the smart-phone market. These miniaturized sensors including GPS receivers, accelerometers, gyrocscopes, brushlesss motors and more, have led to a growing unmanned aerial systems (UAS) industry. The evolving technology has followed patterns similiar to GPS technology in that it was once used exclusively by the military. The commercialization of drones has brought down costs significantly and democratized them for civilian use across many fields and domains. UAS now have the ability to carry lightweight optical sensors for mapping and flights can be programmed with greater autonomous precision than manual piloting, increasing both the quality and reliability of repeat datasets. Combined with Structure-from-Motion based techniques (a key technology from the fields of computer vision and photogrammetry) three-dimensional models that are accurate within centimeters can be constructured over topographic features (Küng et al. 2011; Westoby et al. 2012). Topographic models with precise real-world coordinates can be acquired and compared over a period of time providing a new way to quantify significant changes with fine-scale precision across an active flow field. UAS provide low-cost automated flights that are able to capture very high spatial resolution imagery at low altitude reducing the risk of human life during flights (Harwin and Lucieer 2012).

The work is divided into two major chapters as follows: Chapter 2 focuses on the emplacement processes of pāhoehoe related to the constraints of microtopography, how new

flows modify and invert pre-existing topography and how emerging technologies can improve monitoring efforts and hazards assessments during an ongoing volcanic crisis. We focus on the operational benefits of deploying unmanned aerial systems (UAS) in the context of hazard assessment during flow advancement. Results from the chapter establish a clear need for frequent and updated high spatial resolution digital elevation models (DEM) to improve both short-term hazard and long-term hazard forecasts.

Chapter 3 quantifies the evolution of a stalled pāhoehoe lava flow during a 4-week period, documenting and measuring the growth of feeder tubes, inflation across the flow field, volume, supply rates, and precursors to breakouts. Pāhoehoe morphology is also examined including the evolution of a sinous tumulus over the active tube as is the importance of continous detailed monitoring over large spatial extents with UAS.

Author's Contributions

Nicolas Turner collected the UAS images, secured permission from the FAA for UH Hilo, processed the imagery data for analysis, and wrote the manuscript and this thesis. Ryan Perroy served as PI for the research projects, processed all GPS and ground transect data, provided field personnel, and contributed suggestions to the first manuscript. Ken Hon contributed to the research design, provided insights on pāhoehoe behavior, and critiqued the first manuscript. Sebastien Biasse contributed to inflation figures and interpretations. Bruce Houghton contributed to interpretations of the data and the manuscripts.

Chapter 2

Lava flow hazard prediction and monitoring with UAS: A case study from the 2014-2015 Pāhoa lava flow crisis, Hawai‘i

Published as:

Turner, N.R., Perroy, R.L., Hon, K. (2017) Lava flow hazard prediction and monitoring with UAS: A case study from the 2014-2015 Pāhoa lava flow crisis, Hawai‘i. Journal of Applied Volcanology 6:17. doi: 10.1186/s13617-017-0068-3

2.1 Introduction

Rapid acquisition of high quality topographic data is crucial for monitoring and forecasting lava flow behavior during effusive volcanic crises. Digital Elevation Models (DEMs) are the primary data layer used in models to estimate future lava flow paths and provide flow hazard assessments. The accuracy of the modeled results, either from the paths of steepest descent method (Kauahikaua 2007) or other physics-based lava flow models (e.g., FLOWGO, SCIARA, DOWNFLOW, MAGFLOW), depends strongly on how well the DEM represents the physical environment, which can be difficult to determine in heavily vegetated areas (Harris and Rowland 2001; Crisci et al. 2004; Favalli et al. 2005; Negro et al. 2008). As lava flows change the landscape, subsequent flows will travel along new paths of steepest descent, requiring updated DEMs to reflect the dynamic environment. (Kauahikaua 2007; Favalli et al. 2009).

Here we present work done to generate pāhoehoe lava flow paths, based on high resolution topographic models extracted from unmanned aerial system (UAS) imagery collected over the June 27th lava flow during the 2014– 2015 eruption event near Pāhoa on the island of Hawai‘i. In coordination with Hawai‘i County Civil Defense (HCCD) and the U.S. Geological Survey Hawaiiian Volcano Observatory (HVO), we mapped the pre- and post-flow topography and developed a computational workflow to merge multiple DEMs, filter them of vegetation, and generate projected paths of steepest descent. Future flow paths were also generated to show the impact of the June 27th flow on a potential lava flow in the future that might inundate the area based on the post-flow topography. We compare our UAS-derived results to paths generated from an existing United States

Geological Survey (USGS) 10 m DEM used by responding agencies during the 2014–2015 Pāhoa lava flow crisis.

2.1.1 Lava flow monitoring techniques

Active lava flows are monitored and mapped with a variety of techniques, including ground-based surveys and imagery collected by satellites and manned aerial platforms (Poland 2014; Orr et al. 2015; Patrick et al. 2015). Ground-based surveys employing lidar or visible-light imagery with Structure-from-Motion can collect detailed three-dimensional data, but are limited in their spatial coverage and, in the case of lidar, high cost (Cashman et al. 2013; Hamilton et al. 2013). These limitations make ground-based approaches viable for studying isolated features, as opposed to landscape-scale phenomena. Satellites have become essential platforms for remote sensing of active lava flows, providing datasets of large spatial coverage for hazard monitoring (e.g., Higgins et al. 1997; Wright et al. 2008; Harris et al. 2011; Ganci et al. 2012; Patrick et al. 2016). Intermittent cloud cover, coarse spatial image resolution, and long re-acquisition intervals all present problems for these platforms when monitoring dynamic lava flows. Manned helicopters and fixed-wing aircraft provide high-resolution aerial imagery but are expensive to operate, can have difficulties acquiring consistent data, and are normally restricted to higher flight altitudes (above 150 m) for safety reasons.

UAS technology provides several advantages over satellite, manned aircraft, and ground based surveys for data capture over active lava flows. These advantages include (1) low-cost capability for repeat aerial surveys with high temporal resolution; (2) low altitude flight operations for acquiring cm-scale spatial data; (3) automated mission planning and flight operation for consistent datasets; (4) minimal risk to human life in the event of a crash or accident; and (5) the ability to cover an area in high detail without requiring intensive field operations for personnel (Harwin and Lucieer 2012; Westoby et al. 2012; Hugenholtz et al. 2013). For these reasons, small UAS platforms allow frequent data collection over active flows and can be deployed on short notice.

2.1.2 The 2014–2015 Pāhoa lava flow crisis

Hawai‘i Island’s youngest volcano, Kīlauea, is one of the most active volcanoes on earth. In 1983, Kīlauea began an eruption focused at Pu‘u ‘Ō‘ō that continues to erupt

at the time of writing (April 2018). Between 1983 and 1991, lava flows from Pu‘u ‘Ō‘ō repeatedly impacted communities in East Hawai‘i, burying 184 structures and completely destroying the town of Kalapana. Between 2000 and 2012, an additional 30 homes were destroyed by lava flows to the South-East of Pu‘u ‘Ō‘ō (Kauahikaua et al. 2003; Orr et al. 2013). On June 27th, 2014, a new vent formed on the northeast side of Pu‘u ‘Ō‘ō crater. Pāhoehoe lava from this vent, dubbed the June 27th lava flow, reached the outskirts of the town of Pāhoa in October 2014 and threatened to isolate over 10,000 people in the surrounding area, cutting their ready access to power, water, and critical infrastructure. The June 27th flow continued to threaten communities around Pāhoa until March, 2015, when breakouts ~15 km upslope diverted lava supply away from the front (Poland et al. 2016). The crisis lasted approximately seven months based on disaster declarations, but the June 27th flow was not officially declared inactive until June, 2015.

2.2 Methods

2.2.1 UAS flight operations

Our study focused on the lobe of the June 27th flow active from late December, 2014, to March, 2015. We used a small fixed-wing UAS (SenseFly SwingletCAM) with a modified 16.1-megapixel Canon IXUS 127 HS camera to map micro-topography surrounding the active flow front (Fig. 2.1). UAS flights typically lasted 25 min and the camera payload collected between 100 and 300 geotagged images per flight. We operated under a public certificate of authorization on behalf of the University of Hawaii at Hilo (2014-WSA-60-COA) and under FAA rules that re- quire licensed pilots to keep aircraft within line-of-sight and under 400 ft. (122 m) above ground level (AGL). UAS flights were flown in a grid pattern with 80% frontal and 75% side overlap between image footprints. The camera was triggered autonomously using the onboard flight controller. Each trigger point was pre-determined based on the uploaded flight plan using eMotion2 flight planning software. Flights were monitored in real-time via visual observers and a radio telemetry (2.4 GHz) link from a laptop computer.

During the Pāhoa crisis, HCCD erected a temporary flight restriction (TFR) around the active flow front, restricting all manned and unmanned aircraft to those directly supporting relief operations. We were granted access to the TFR airspace after receiving

permission from both the FAA and Civil Defense with our public Certificate of Authorization and secured ground access from land owners and stakeholders within the study area. During flight operations, we communicated with nearby aircraft using a ground-to-air aviation radio and kept a distance of 1000 ft. (305 m) horizontal and 500 ft. (152 m) vertical to other aircraft. These precautions were import- ant for safely integrating UAS into congested airspace where multiple tour helicopters frequented the outskirts of the flow every hour.

Maintaining direct line of sight with the UAS at all times, as required by FAA regulations, was challenging for operational planning, as the lava flow was surrounded by thick forest with canopy heights >7 m. Flight operations were conducted from new fire-breaks surrounding the perimeter of the flow (Fig. 2.1) and other clearings. A total of 5,581 aerial images were collected from 23 UAS missions between December 14, 2014 and July 26, 2016.

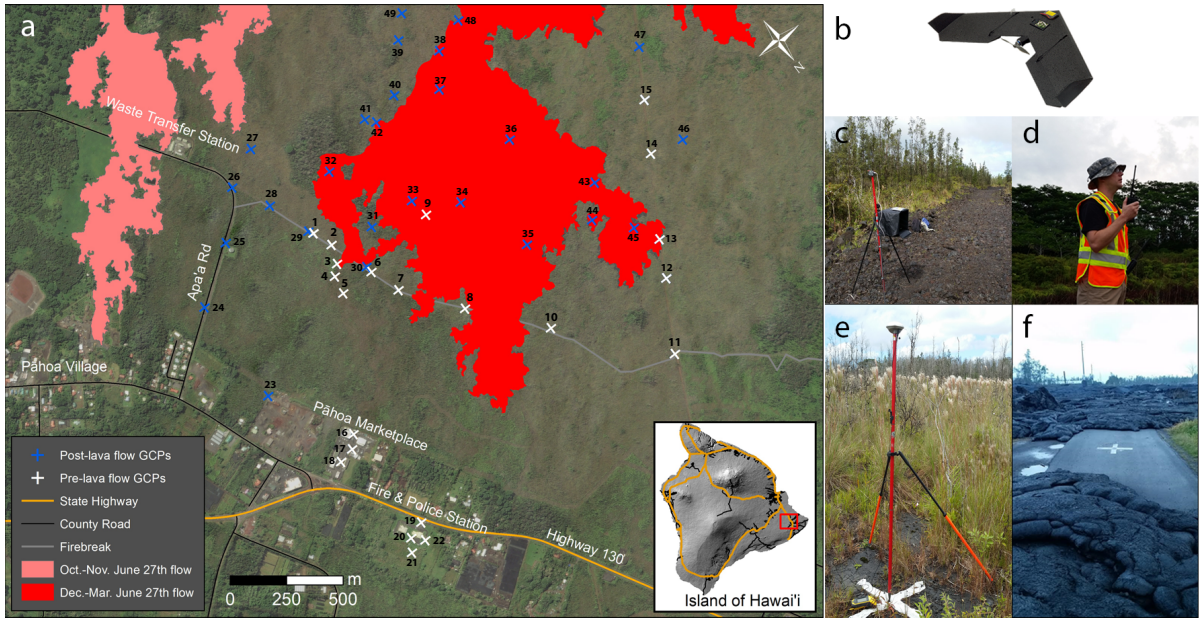

Fig. 2.1 **a** Map displaying the June 27th flow footprint near the town of Pāhoa. Ground Control Points (GCP) depicted as white crosses (pre-flow GCPs) and blue crosses (post-flow GCPs) with corresponding numbers. In early December, 2014, the County bulldozed a firebreak to contain wildfires sparked by the lava flow. The firebreak provided access to the densely vegetated area for placing GCPs and conducting UAS flights. **b** UAS fixed-wing aircraft used in this study (SenseFly SwingletCAM) **c** Ground control station including laptop, radio telemetry modem, sun-shade box, and tripod. **d** UAS crew member communicating with nearby aircraft using a two-way aviation

VHF radio. **e** Obtaining GCP geographic coordinates with a differential GPS Trimble Explorer 6000 unit and Zephyr external antenna. **f** June 27th flow surrounding a GCP.

Prior to the flights, we placed a series of ground control points (GCP) across the flow field study area to provide positional control and to georeference our UAS imagery and derived DEMs (Fig. 2.1). The three-dimensional coordinates (WGS84, UTM Zone 5 N) for GCP locations were surveyed using a Trimble Geoexplorer 6000 differential GPS with a Zephyr model external antenna mounted on a 2 m pole (Küng et al. 2011; Westoby et al. 2012). Occupation times with the Trimble GPS averaged 10 min and data were post-processed with Trimble Pathfinder Office software using nearby CORS stations. Based on the differential correction report, 71.5% of the corrected positions had an accuracy of 5–15 cm and 99.1% had an accuracy of 30–50 cm or better. Overall, 49 GCPs were deployed across the roughly 5.87 sq. km study area and at least 5 GCPs were included in each UAS flight, distributed across the flight coverage area as evenly as possible. Please refer to Table 1 Appendix A for corresponding flights and GCPs used.

To independently assess the accuracy of the UAS derived DEM, an additional 32 points were surveyed across the study area via GPS. These points were collected using the previously described survey technique but were not included in the UAS image processing steps. Based on the differential correction report for these data, 75.35% of their corrected positions had an accuracy <5 cm and an additional 24.65% had an accuracy be- tween 5 and 15 cm. Absolute elevation values from the GPS survey were then compared to extracted elevation values at the same XY positions for the UAS-derived 1 m DEM and an older 10 m DEM of the Puna district, acquired from the USGS National Elevation Dataset (NED) program and used during the active disaster operations.

2.2.2 Data analysis and processing

An overview of the data processing and analysis workflow is shown in Fig. 2.2. Imagery and GCP coordinates were processed using structure-from-motion (SfM) software Pix4D Mapper Pro (v2.1.61, Zurich, Switzerland) to generate a high density digital point cloud from each flight. SfM software identifies matching features in an image and extracts three-dimensional points based on multiple geometric views of the same object in the scene by using overlapping photographs (Küng et al. 2011; Westoby

et al. 2012). The point clouds from each flight were merged into a single dataset based on the image acquisition date. Flights conducted between Dec 16, 2014 and Jan 18, 2015 were combined and used to generate a 1 m DEM with 0.1 m vertical resolution for pre-flow analysis. Data from UAS flights conducted between Jan 18, 2015 and March 25, 2015, after the completion of the lava flow event, were used to generate a similar DEM for post-flow analysis.

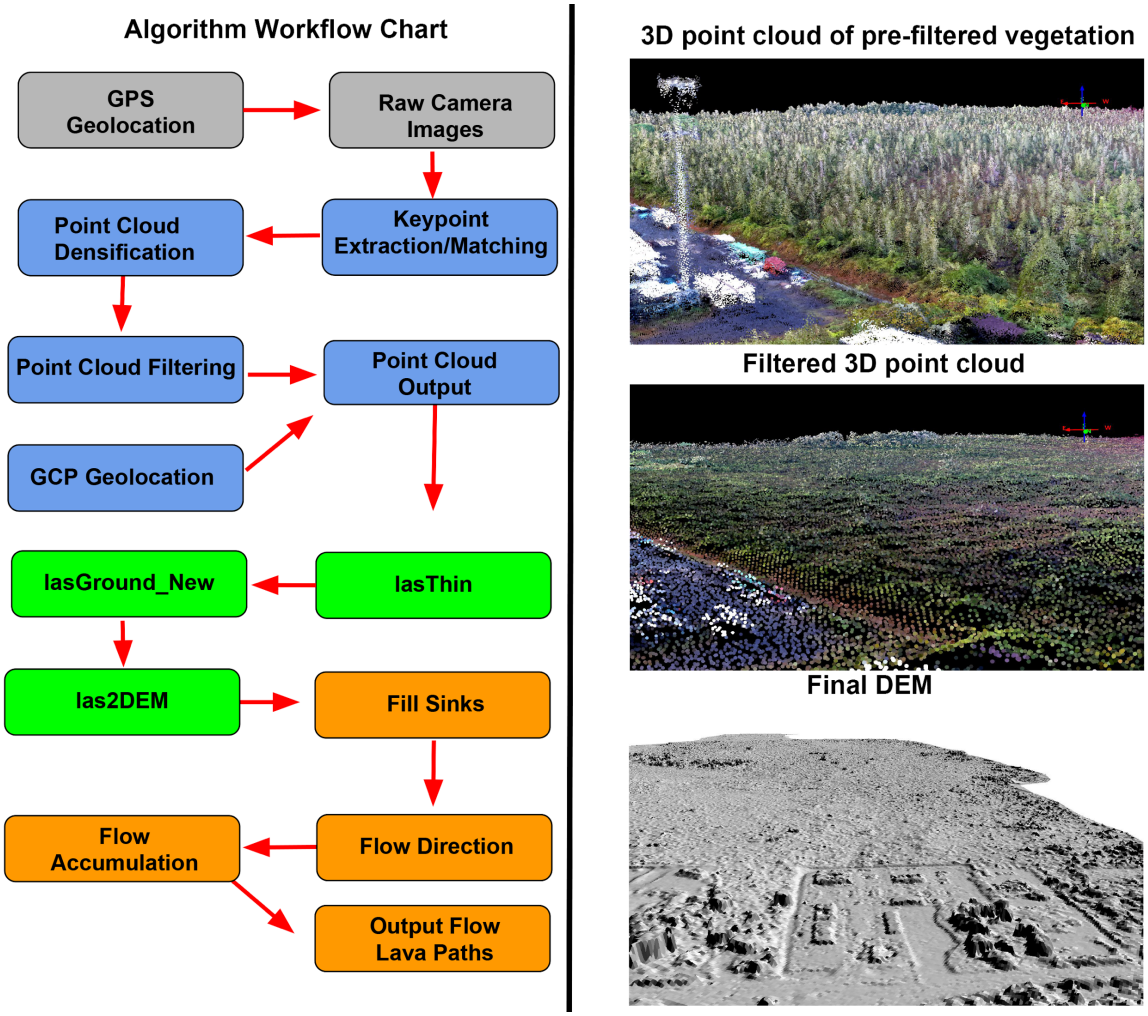

Fig. 2.2 Left Side: Flow chart summary of the processing workflow beginning with raw aerial images geotagged with onboard GPS (grey); Structure-from-Motion software processing steps (blue); digital point cloud filtering using LAStools (green); DEM processing to extract paths of steepest descent via ArcGIS hydrology workflow (orange). Right side: (top) raw point cloud before any filtering, (middle) filtered point cloud following removal of vegetation and other structures, (bottom) Hillshade representation of "bare-earth" DEM generated from the filtered point cloud.

Bare-earth elevation models filtered of vegetation were required for the determination of accurate flow paths. Because passive optical remote sensing techniques rely on reflected light, dense foliage and canopy shadows can conceal the complex topography lying underneath (Dandois et al. 2015; Fraser et al. 2016). In order to generate bare-earth DEMs of the study area, situated within a lowland tropical forest landscape, we needed to filter out surface features such as buildings and vegetation. We employed point cloud filtering techniques using LAStools (rapidlasso GmbH), a lidar software package consisting of a series of powerful batch script algorithms to process point cloud data. The following is a detailed description of the parameters and settings used for each script in LAStools to extract the bare-earth elevation values by filtering the point clouds of vegetation (highlighted in green on Fig. 2.2). Please refer to cs.unc.edu/~isenburg/lastools/ and Isenburg et al. 2006 for additional information. We employed the (1) lasThin tool to thin the point cloud, keeping only the lowest elevation points within each 1 m grid size; (1) lasGround_New tool for bare-earth extraction, classifying the points into ground points (class = 2) and non-ground points (class = 1) using a step size of 1 m (town or flats setting) and an initial search for ground points as '-fine'; and Las2DEM tool to produce a continuous bare-earth digital elevation model (DEM) from the point cloud using the remaining elevation values at a step size of 1 m and exported as a tiff raster format. We chose a 1 m grid size for our pre-flow raster because finer grid sizes detected too much vegetation, which interfered with generating a low-noise DEM from which paths of steepest descent could be generated. Processing time for SfM models typically took several hours on an ASUS computer (CPU: Intel Core i7 3.0 Ghz; 32GB RAM; GPU: NVIDIA Geoforce GTX 970) with additional time required to filter vegetation and run flow path calculations (1–2 additional hours). Pre-lava flow paths were calculated from the DEM generated by UAS over- flights in early December, 2014, after an upslope breakout formed a new lobe that ran parallel to the original flow margin and cut off lava supply to the original flow front (Poland et al. 2016; Patrick et al. 2016). Alternative point-cloud processing software or programming libraries (e.g., CloudCompare, QT Modeler, MATLAB, OpenCV) could also be used in place of LAStools.

Tools to calculate paths of steepest descent are common in many Geographic Information System (GIS) software packages, usually falling under hydrology toolsets. For

a more detailed discussion on how these paths are calculated please refer to Tarboton et al. 1991; Kauahikaua 2007. The pre-flow DEM was brought into ArcGIS (v10.2) where paths of steepest descent were calculated based on the lavashed concept (Kauahikaua et al. 1995) with the following hydrology workflow: (1) we filled sinks throughout the DEM to ensure proper delineation of stream networks; "sinks" are often errors in the DEM due to rounding of nearest integer values and need to be filled to avoid a discontinuous drainage network; (2) flow direction was calculated using the filled DEM as input in the Spatial Analysis extension and (3) flow accumulation was generated using the flow direction DEM. The final paths of steepest descent were based on the 1 m DEM.

The same workflow was used to produce a filtered 1 m spatial resolution post-lava flow DEM, using imagery collected after the effusive event was over. We also used this same workflow on the USGS 10 m DEM (Fig. 2.3, blue lines). The 10 m bare-earth USGS DEM was the highest-resolution elevation dataset publicly available at the time of the event and was derived from USGS 7.5′ minute DEM Quads produced by the National Elevation Dataset (1983). USGS and Civil Defense utilized helicopter and ground surveys to produce a series of maps depicting the flow's outline and evolution during the crisis. We compared our projected paths of steepest descent to the lava flow's actual progression using a time-series of flow outline GIS polygons provided by the USGS and Civil Defense.

We also examined the impact of DEM spatial resolution on lava flow paths. This was done by resampling our UAS-derived DEM at progressively coarser resolutions, up to 10 m resolution in 1 m increments, and calculating the resulting paths of steepest descent at each step using a comparable flow accumulation threshold (Jenson and Domingue 1988). Like hydrologic watershed boundaries for stream networks, the contributing areas of potential lava flow paths can be delineated based on topography. Lavasheds represent the area in which a given flow path can be identified and serve as a way to identify possible paths of steepest descent at varying resolutions (Kauahikaua et al. 1995). Calculating these lavasheds can provide a more synoptic view of the potential paths a flow may travel within a confined geographic area. Lavasheds were calculated using the ArcGIS watershed geoprocessing tool, and pour points were set at every fork between paths of steepest descent to produce one lavashed per path. To quantify the ratio

of flow length and total area of a unit watershed, the length of each flow path per lavashed unit was divided by the total area of that given lavashed unit. The mean of all lavashed areas and flow lengths were determined for each DEM. The flow path length / lavashed area was then converted to a logarithmic scale with a base of 10.

2.3 Results

A key component of this study was to determine how well the UAS-derived DEMs performed in terms of characterizing the landscape and supporting lava hazard predictions. Paths of steepest descent were generated from our UAS-derived 1 m bare-earth DEM (pre-flow) and the USGS 10 m DEM used during the active disaster operations and overlain against the time-series of flow field outlines mapped by Hawaiiian Volcano Observatory (Fig. 2.3). The elevational accuracy of the two DEMs, as measured against a differential GPS survey of 32 independent points distributed around the study area, was determined and found to be quite similar, with an RMSE value of 0.69 for the 1 m DEM and 0.74 for the 10 m DEM (Fig. 2.4).

Results from the resampling experiment to determine the effect of DEM spatial resolution on paths of steepest descent and lavashed delineation are shown in Fig. 2.5. Individual lavasheds are outlined in black within the larger orange polygons, with lines of steepest descent depicted as yellow lines. As the number of possible lavasheds decreases with coarsening spatial resolution, the flow path length for each path of steepest descent within a given lavashed unit decreases as well (Fig. 2.5).

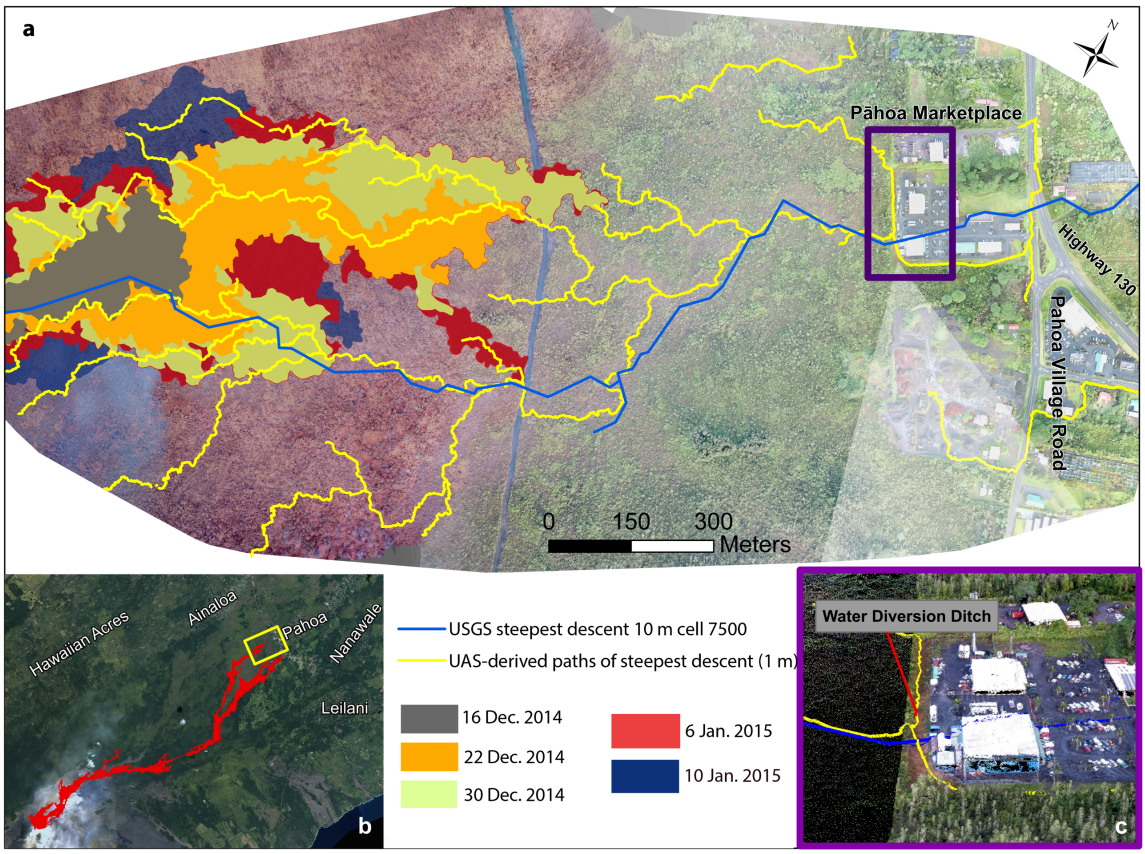

Fig. 2.3 a Comparison between 1 m UAS-derived flow paths (yellow lines) and 10 m USGS DEM (blue lines). The advancing lava flow depicted as a series of flow outlines produced from HVO field mapping from Dec. 16, 2014 through Jan. 10, 2015. The 1 m UAS flow paths were generated from data collected on Dec. 16, 2014- Dec.17, 2014. The purple box highlights the area of panel c. b Final extent of the June 27th flow. c UAS-derived 3D point cloud showing the 5 m ditch surrounding the Pāhoa Marketplace, a topographic feature that was not identified from the 10 m USGS DEM due to coarse spatial resolution.

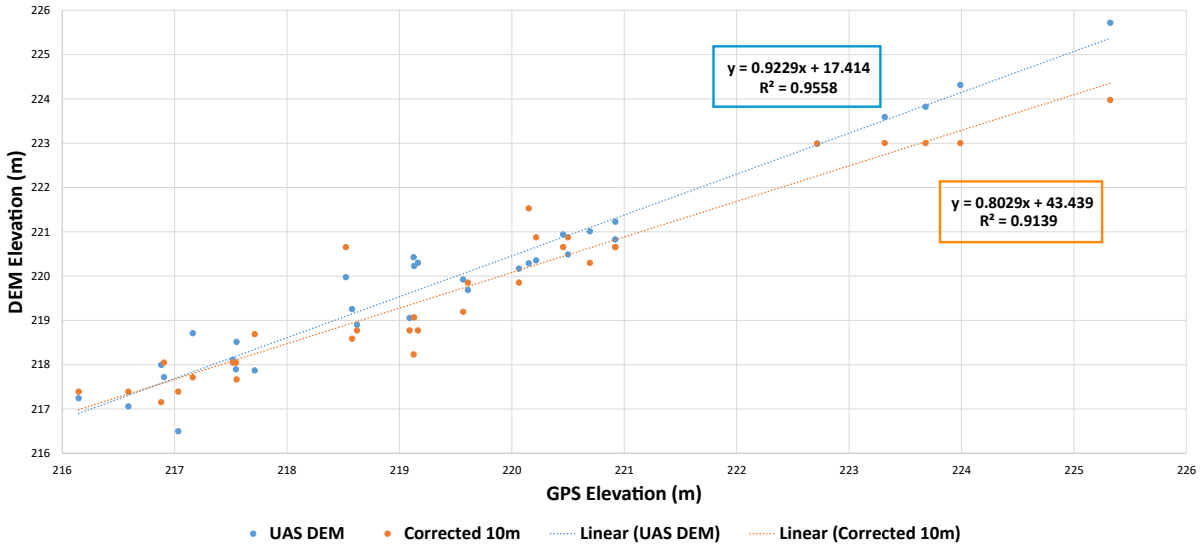

Fig. 2.4 Elevation values from an independent GPS survey of 32 points collected within the area of the pre-flow DEM plotted against elevation values extracted from the 1 m UAS-derived DEM (blue dots) and the 10 m USGS DEM (orange dots).

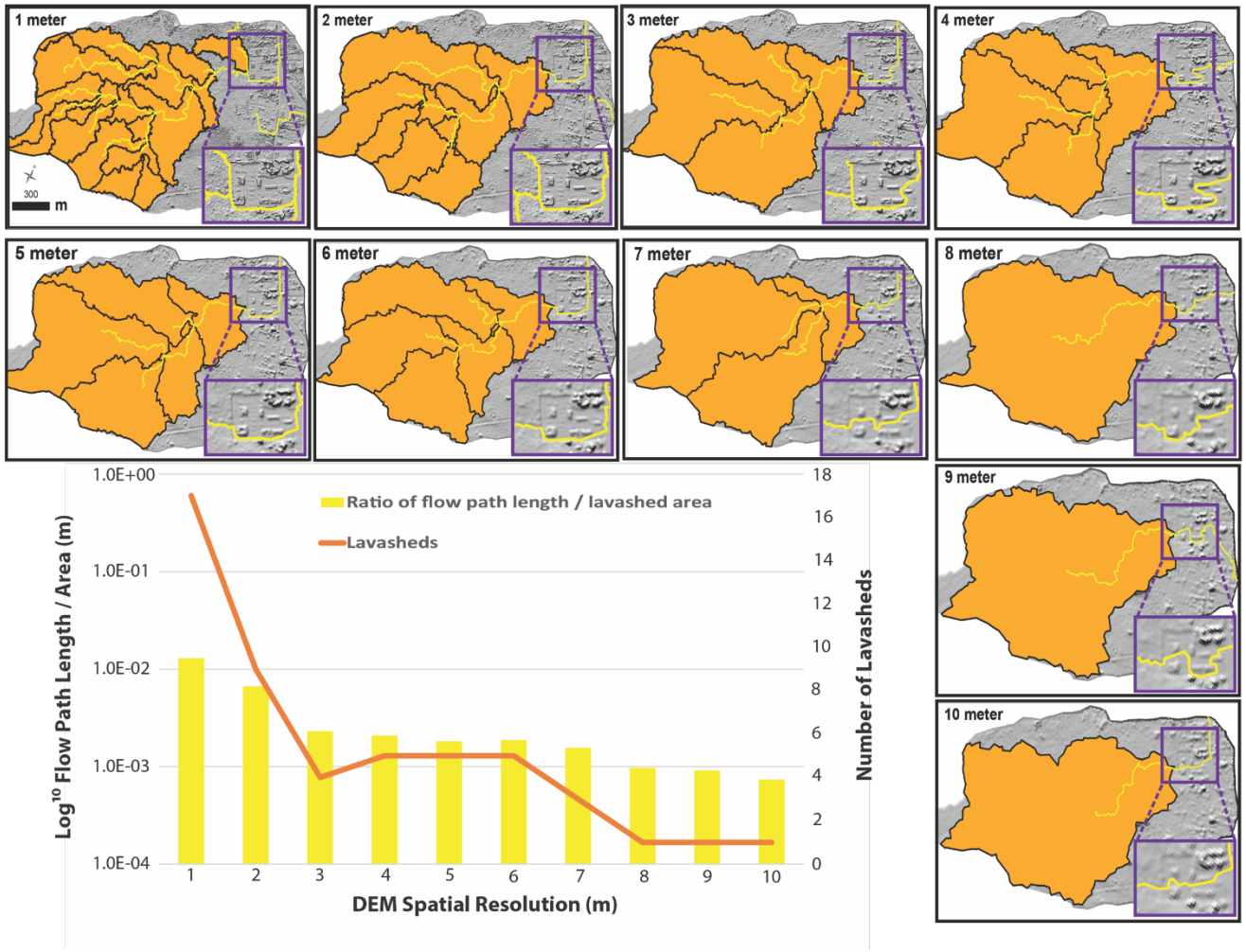

Fig. 2.5 Resampled UAS-derived DEMs showing the loss of detail with coarser resolution data depicted in the varying lavasheds (orange) and the total length of flow paths in a given lavashed. Within each lavashed inset is a blow-up of the 5 m ditch surrounding the Pāhoa Marketplace. The 5 m ditch was excavated during construction of the Pāhoa Marketplace in 2004. Graph showing the step-wise series of DEMs decreasing in spatial resolution from 1 m to 10 m, the effect on total lavasheds per DEM and the ratio of flow length path / lavashed area.

2.4 Discussion

2.4.1 Implications for lava flow monitoring

The short-term behavior of long-lived pāhoehoe flows is difficult to predict, as advancing lava is influenced by new breakouts at the front or along the margins of an active flow and requires a continuous supply of new lava through the molten core (Kauahikaua et al. 1998; Hamilton et al. 2013). During the Pāhoa lava flow crisis, early forecasts of flow behavior were thwarted by hidden ground cracks in the Puna forest

reserve (Poland et al. 2016). Accurate and up-to-date measurements of underlying topography are crucial for flow behavior analysis, and are a critical gap in eruption monitoring that UAS can fill.

An example of this can be seen around the Pāhoa Marketplace, built in 2004, where the NED 10 m DEM flow paths pass directly over a 5 m wide water diversion ditch surrounding the development (Fig. 2.3). The primary reason this occurs is because the 10 m DEM was generated prior to the construction of the Pāhoa Marketplace and excavation of the drainage ditch. A second reason is due to the coarseness of the 10 m DEM. Based on our resampled DEM experiment (Fig. 2.5) we see that DEMs with a resolution >6 m do not pick up this feature, while UAS-derived DEMs with a resolution below 5 m produced flow paths that recognized the water diversion ditch. While it is unclear how or if the ditch would influence final emplacement of the flow, it is a substantial topographic feature that coarser datasets, even up-to-date ones, do not detect. Higher spatial resolution DEMs allow for a higher number of lavasheds to be detected (Fig. 2.5), making them valuable for short-term hazard assessments.

Fortunately, the June 27th lava flow stopped short of overrunning Pāhoa and stagnated by March, 2015, eliminating the threat to nearby communities. However, scientists and emergency planners concerned with future lava flows can benefit from long-term hazard planning using UAS datasets. Post-flow modeling using UAS derived data shows the influence of the 2014–2015 flows on diverting the paths of future lava flows into completely new directions (Fig. 2.6), making lava flow hazard studies based on the pre-flow DEMs obsolete. To help improve response efforts for future lava flows, acquiring more recent and higher resolution DEMs would benefit any region previously inundated by lava flows Additional insight on the future behavior of a flow could be gleaned by finding the critical threshold at which a pāhoehoe flow will jump between given lavasheds (Fig. 2.5) based on flow parameters such as size, mass flux, and surrounding topography. How important the boundaries of a given lavashed are in constraining the direction of a flow will depend greatly on the current stage of maturity in an ongoing eruption, the type of flow (e.g., sheet flow, hummocky tube-fed flow), current topography, and the context of the response efforts (short-term or long-term hazard planning). High resolution DEMs can provide important information towards

observing the boundary at which flow paths diverge (Hon et al. 1994; Hamilton et al. 2013).

Lava flow monitoring with UAS can provide high spatial resolution DEMs with the capability for frequent and cost-effective overflights to reflect new changes caused by flow activity. The datasets provide a detailed record of morphological changes across the flow field, serving as a time-series digital repository of observations on pāhoehoe behavior. This can be of high importance during a prolonged effusive crisis because eruptions can span weeks to years, and budget limitations control the frequency of helicopter overflights to monitor lava flows (Patrick et al. 2016; Orr et al. 2015b). A key observation from a HVO study on the 2014–2015 flow showed a large percentage of surface activity occurring away from the immediate flow front in the form of lateral breakouts well behind the active front (Patrick et al. 2016), underscoring the importance of extending the operational range of UAS to capture areas beyond the active front of an advancing pāhoehoe flow. Doing so would extend the benefits of higher spatial and temporal resolution across the entire flow and throughout the flow's evolution.

2.4.2 Applications for other lava flow models

This work has focused on the lines of steepest descent technique, one of the simplest methods for predicting lava flow paths (Kauahikaua 2007). However, more sophisticated lava flow modelling efforts, including stochastic slope-controlled models (Harris and Rowland 2001; Favalli et al. 2005), cellular automata models (Crisci et al. 2004; Del Negro et al. 2005; Vicari et al. 2007), and other numerical simulations (Dietterich et al. 2015), also rely on high quality DEMs input layers to produce successful results. UAS provide a means of effectively generating these needed DEMs, regardless of the modeling method. For models that are computationally complex, simulation run time is an important factor to consider for the results to be of value, especially during an active crisis that demands quick and frequent updates to changing conditions. The ability of UAS to rapidly and continuously update changes in topography can reduce or even negate the requirement for running multiple flow paths in a stochastic simulation. Beyond collecting the UAS data, an important aspect of effectively incorporating this technology into hazard operations will come from automating the DEM post-processing steps (e.g., vegetation filtering,

combining multiple flights) as much as possible to make new DEMs more readily accessible for given scenarios.

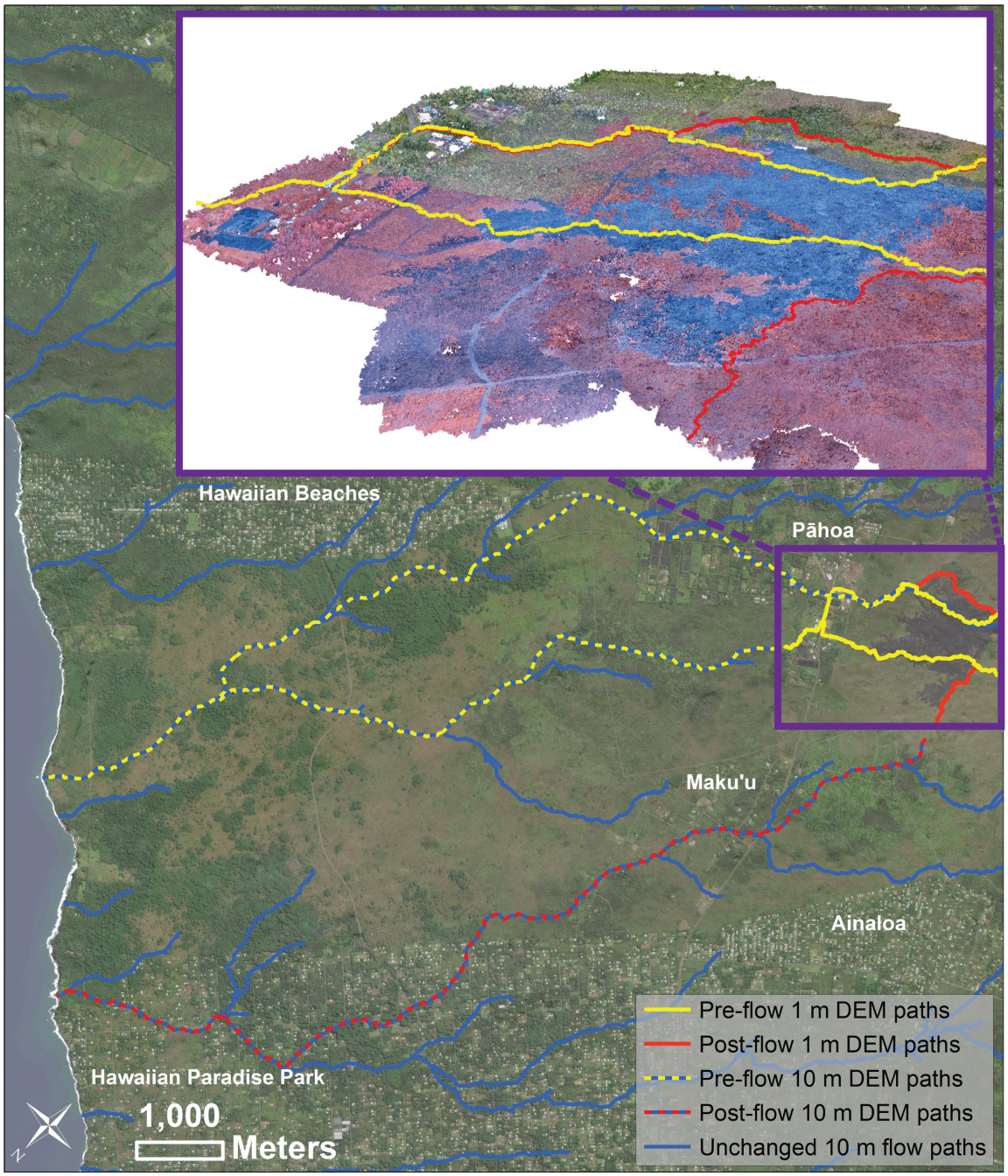

Fig. 2.6 Comparison of the pre-lava flow paths the June 27th flow would have followed (pre-flow solid yellow lines based on UAS 1 m DEM, pre-flow dashed yellow and blue lines based on 10 m DEM) to the new paths future flows will follow (post-flow solid red lines based on UAS 1 m DEM, post-flow dashed red and blue lines based on 10 m DEM). Purple box delineates boundary of 1 m DEM; outside of this the unchanged USGS 10 m flow paths are shown in blue. Puna

communities are labelled by region. The deflection of new flows (purple boxed panel) now poses a greater hazard to communities of Maku'u and Hawaiian Paradise Park.

2.4.3 Successful volcano monitoring with UAS

The successful integration of UAS into active volcano monitoring programs still has challenges, including evolving aviation regulations. In the United States, the Federal Aviation Administration has released its small UAS regulation Part 107, which permits UAS flights by pilots that pass a remote pilot exam. Waivers can be acquired to do special types of flying such as night operations, flying beyond line-of-sight (BLOS), and having a single UAS pilot control multiple aircraft simultaneously commonly referred to as SWARM flights (Diaz et al. 2015). For most eruption settings, large-scale monitoring over the length of the entire flow field will require BLOS flying and/or the use of SWARM technology with multiple UAS mapping sections of the lava flow simultaneously. In the future, these types of operations can significantly enhance the monitoring capability of volcano observatories worldwide within existing monitoring programs. In addition, UAS-derived topographic datasets can be easily combined with other monitoring tools such as thermal infrared mapping and field-based measurements of pāhoehoe flow inflation and advancement (Patrick et al. 2016). The increased mapping frequency UAS flights afford, due to their low operational costs, can be a substantial boost to effective monitoring and tracking of both pāhoehoe and a'ā lava flows at effusive volcanoes worldwide.

During response efforts for the Pāhoa crisis, all imagery and related data products from this project (DEM, orthomosaics) were shared with both emergency managers at Civil Defense and scientists at HVO. Although UAS data were shared as quickly as possible, final delivery of data products often took 1–2 days due to field logistics, travel time, computational processing, and coordinating with Civil Defense analysts. If UAS are to be used effectively in a future crisis, increased data workflow automation can prevent staleness of information. Other advancements in UAS technology, including connecting field operations to the internet via cloud related hardware, can allow field teams to share imagery in near-real time. Structure-from-Motion processing could be done in the cloud or imagery downloaded locally to be processed before teams even leave the field. Other approaches include computer vision based machine learning models to extract only the most relevant information from UAS imagery (e.g.,

classifying and extracting fresh lava), reducing bandwidth requirements and transferring only the most critical data during flight. If placement of GCPs are too dangerous for UAS crews, other technologies such as high precision real time kinematic (RTK) GPS or omitting GCPs entirely and sacrificing DEM accuracy are possible alternative approaches. The most successful future integration of UAS for volcano monitoring programs will likely include all of the above as observatories supplement existing monitoring networks (e.g., seismic networks, GPS stations, gas monitoring, weather stations) with UAS technology.

2.4.4 Additional applications for UAS in lava flow monitoring

Beyond continuous updates to changes in topography and generating high resolution DEMs, products derived from this work can be used to gain additional insights into the emplacement processes of active pāhoehoe flows, including detailed measurements of lava flow inflation rates, flow thickness, volumetric flow rates, and characterization of features (e.g., tumulus formation, surface vs lateral break-outs, sinuous inflation ridges, hummocky vs sheet morphology, lava partitioning) over spatially and temporally useful scales to improve emergency response efforts (Perroy et al., 2015). Consecutive Structure-from-Motion derived three-dimensional surface models of the flow, collected over hours to weeks, can effectively track the advancement of a flow, formation of a master tube system, and related breakouts. Merging these datasets with aerial thermal infrared imagery captured contemporaneously may yield new insights into flow emplacement behavior (Patrick et al. 2016).

UAS technology can provide a detailed synoptic view of a flow's evolution and emplacement behavior, possibly spurring the development of new predictive models designed specifically for pāhoehoe lava flows. These models will need to incorporate the complexity of an actively evolving flow field including the development of a master tube system prone to leakage, identify the morphology of breakouts (e.g., sheet and hummocky lava), reflect changes in lava supply/storage through inflation rates, and rapidly update the modifications in topography. UAS provide the capability to collect this type of data both spatially and temporally.

2.5.1 Conclusions

We demonstrate a new approach to generating updated pāhoehoe lava flow paths, based on high resolution topographic models extracted from unmanned aerial system (UAS) imagery during the 2014–2015 Pāhoa lava flow crisis. UAS provide a means of rapidly assessing changing field conditions and reducing the uncertainty in lava flow behavior based on topographic constraints. This ability can make a significant difference for hazard mitigation efforts by calculating new paths of steepest descent immediately following alteration of the physical environment. The repeat collection of digital x-y-z point cloud data can be used for long-term monitoring and analysis of lava flow evolution. The potential benefits of UAS in repeated deployments over active lava flows include:

(1) Generate high spatial resolution DEMs from low-altitude UAS flights using low-cost optical sensors.
(2) Better estimate future flow path behavior and reduce uncertainty in hazard forecasts.
(3) Improve the frequency and quality of data collected by volcano monitoring programs, due to the low operational costs of UAS and their ability to fly on short notice.
(4) Capture new topographic changes caused by pāhoehoe flow inflation, providing detailed updates to obsolete topographic datasets that were not possible before.
(5) Supplement existing remote sensing (e.g., satellite and manned aircraft) and field based monitoring of active flows.

As UAS technology progresses and matures, we believe future monitoring efforts that utilize UAS will fill a critical gap in volcano monitoring. UAS hold great potential for improving response efforts during a volcanic crisis and are an effective tool for mapping changes for both short-term and long-term lava flow hazard assessments.

Chapter 3

Inflation and emplacement dynamics during the 2014-2015 Kīlauea lava flow: Perspective from use of an unmanned aerial system

3.1 Introduction

Pāhoehoe lava flows cover much of the earth's surface and often form systems of complex, interconnected tube pathways via flow inflation. The importance of pāhoehoe flow fields to volcanology was evident early, with numerous studies characterizing geometry and morphological features across flow fields (Macdonald 1953; Walker 1991). More quantitative depictions of pāhoehoe behavior started to appear in the 1990's, detailing constraints on surface cooling and inflation rates on the Kalapana flow fields, Hawaii (Mattox et al. 1993; Hon et al. 1994; Peterson et al. 1994; Kauahikaua et al. 1998; Self et al. 1998). These and other papers show that pāhoehoe growth is a complex balance between 1) advancement of the flow front, 2) lateral breakouts behind the front and 3) inflation of the flow. For this reason, pāhoehoe behavior is notoriously difficult to characterize across larger spatial scales especially when activity is widespread and flows occur in branching concealed tube systems. The use of low-altitude unmanned aerial systems (UAS) offers a chance to obtain quantitative data on spatial and temporal resolutions not previously possible with these lavas.

3.1.1 Processes of flow advancement and implications for hazard management

The advance of pāhoehoe flows often slows or stalls on gentle terrain (<~2°) where lava transported through insulated feeder tubes will favor vertical thickening (inflation) and lateral widening of the flow margins. Inflation occurs broadly across the entire flow, but is most concentrated over the interconnected pathways. The location and dimensions of these preferred pathways are controlled by complex factors including slope gradient, viscosity, yield strength, variations in lava supply, either at source or due to short-lived blockages in the tubes, inflation rates, and the geometry of the feeder tubes themselves based on pre-existing topography (Kauahikaua et al. 1998, 2003; Self et al. 1998; Anderson et al. 2012; Dietterich et al. 2012). Lava tubes are prone to leakage and periodic breakouts at seemingly random locations along the margins of the distributary network of pipes. These breakouts can take the form of surface breakouts on top the original flow adding new volume or lateral breakouts which can add to the total area and widening of the flow (Mattox et al. 1993; Orr et al. 2015; Patrick et al. 2017).

During a volcanic crisis if a lava flow threatens nearby communities, anticipating future flow activity becomes the central focus of monitoring scientists. Accurate forecasts are entirely dependent on detailed monitoring, through a variety of methods, of critical parameters, including total final volume and velocity of supply. A critical, but difficult parameter to estimate is the effusion rate of a given flow. This is often derived through inflation growth rates and partitioning of new mass across the flow. Ground-based methods rely heavily on locating skylights, which expose the lava pathway (to be successful), (Kauahikaua, J., et al. 1996) and these are not always available. Satellite-based methods are limited by coverage, spatial resolution, and temporal resolution (Higgins et al. 1997; Wright et al. 2008; Harris et al. 2011; Ganci et al. 2012;).

Here we present the first use of low-altitude UAS to quantify pāhoehoe inflation, breakouts, and rheology using 3-Dimensional models, based on Structure-from-Motion, of the evolving flow front during the 2014-2015 Pāhoa lava flow crisis. Flow models were filtered for vegetation, partitioned by date of emplacement, and step-wise changes in volume were calculated from Oct. 31, 2014, when the active flow front first reached the outskirts of Pāhoa town, to its eventual demise after being robbed of supply ~4 weeks later (Nov. 24, 2014). Furthermore, we quantified changes in morphology which served as precursors to significant inflation along the active feeder tube before a surge in supply induced lateral simultaneous breakouts on both margins of the flow.

3.1.2 Background

3.1.3 The current eruption

Kīlauea has erupted almost continuously since 1983, covering more than 142 km^2 of land and creating 222 ha of new land. The majority of these flows have travelled to the south of Puʻu ʻŌʻō (the dominant vent during this eruption on the East Rift Zone (ERZ)) for ~10 km where they poured into the Pacific Ocean forming lava deltas and adding new land to the Island of Hawaiʻi. Some of these flows have been quite destructive and are responsible for claiming 215 structures including most of the village of Kalapana in 1990 (Orr et al. 2013; Poland et al. 2016). A change in the pattern of eruption began in late May 2014; tilt and GPS stations at the summit of Kīlauea showed an increase in inflation (Poland et al. 2016).

3.1.4 The June 27th lava flow

On June 27th, 2014, HVO reported new eruptive fractures that opened on the northeast flank of Puʻu ʻŌʻō. The new vent system diverted lava to the northeast of Puʻu ʻŌʻō where it

travelled through an extensive network of cracks and dense forest along the ERZ. The new flow was named the June 27th lava flow and by August 24, it emerged from the crack system 11.4 km away from its source vent. After several more weeks the flow approached the outskirts of a rural residential neighborhood called Kaʻohe Homesteads. At this point the County of Hawaiʻi declared a state of emergency and began activating disaster preparedness plans. The flow bypassed Kaʻohe Homesteads which was located on a slight rise and instead followed a drainage path towards the town of Pāhoa, the major population center for the Puna district. By October 25, the June 27th flow crossed Cemetery Road and an electrical transmission line (Figure 3.1), passing through a cemetery and pasture field before stalling within meters of a berm (barrier of soil and cinder) built by a nearby resident and ~150 m from the main street of Pāhoa. Through October 31 and the month of November (the period for this study) the flow front remained stalled, but it continued to inflate and widen laterally by breakouts. By November 24, a surge in lava supply forced a large breakout ~6 km upslope of the flow front. This breakout starved the original flow and it continued down a new drainage path towards the Pāhoa Marketplace. This new arm of the June 27th flow continued to stall, advance, and widen through February 2015. The flow finally stalled ~500 m from Highway 130, the only link between lower Puna and the rest of the island. In mid-March a surge-triggered breakout near Puʻu ʻŌʻō robbed supply from the flow front. These new breakouts remained near Puʻu ʻŌʻō for the remainder of life of the June 27th flow. By May 24, 2016, new flows dubbed 61f and 61g switched to the south of Puʻu ʻŌʻō towards the Pacific Ocean. The 61g flow remains active at the time of current writing (February 2018).

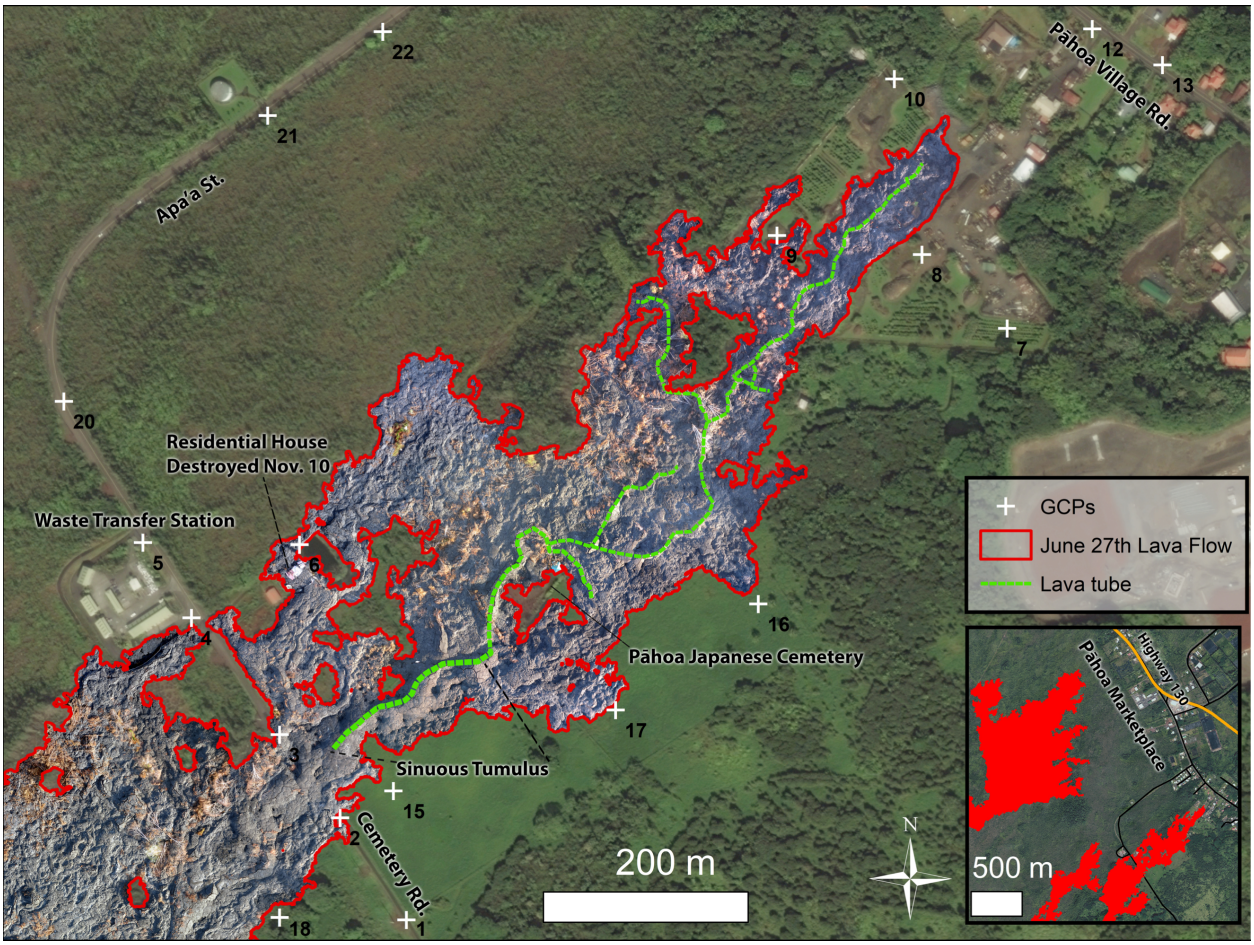

Figure 3.1. Study site showing key landmarks (labelled), June 27th lava flow outlined in red. Lava tube system (dashed green lines) was inferred using features from DEM, cumulative inflation, and orthoimagery. Ground control points (GCP) are shown as white X across study site.

3.2 Methods

3.2.1 UAS flight operations

Our study focused on the distal stalled portion of the June 27th flow between October 31, 2014, to November 24, 2014. A small fixed-wing UAS (SenseFly SwingletCAM) equipped with a modified 16.1-megapixel Canon IXUS 127 HS camera was used to repeatedly map the study region (Figure 3.1). Flights were kept below 400 ft (122 m) Above Ground Level (AGL) and usually lasted for 25 minutes, collecting up to 300 geotagged photos per flight. Automated flights were flown in a lawnmower pattern with 80% overlap. Prior to UAS flights a series of ground control points (GCP) were placed around the perimeter of the flow to provide positional control

and help align disparate datasets. GCPs were surveyed with a Trimble GeoExplorer 6000 unit with a Zephyr model antennae. Additional details on flight operations can be found in Chapter 2.

On November 6, 2014, we conducted several ground-based transect lines using differential GPS and laser mounted total stations. Ground transects were used as a quality check for the UAS derived-DEMs. Ground transects were tied to Benchmark HVO 89-110 and collected in Hawaii State Plan (HSP) coordinates, Zone 1. Transect points were input into AutoCAD 2009 for manual horizontal and vertical translation and then converted from HSP to UTM, Zone 5N. All GPS data were processed in UTM, Zone 5N and based on the differential correction report, 95% of points had a reported accuracy within 0-5 cm. The first ground-survey and UAS flight began at 07:13 (HST). The ground survey was 55 m in length and traversed from the edge of the active flow just after the Japanese Pāhoa Cemetery (Figure 3.2) and ended on the opposite margin of the flow. The transect lines were pinned and marked with spray paint to aid repeat surveys. UAS flights were launched simultaneously to minimize offsets due to ongoing changes in topography. Surveys were spaced at 2 hour intervals with the final survey conducted at 16:16 (HST).

3.2.2 Data processing workflow

Images from each flight were processed with Structure-from-Motion software Pix4D Mapper Pro (v2.2.61, Zurich, Switzerland) to generate high-density digital point clouds. Some of the earlier datasets (e.g., October 31) lacked sufficient GCP coverage and required a special approach to avoid spatial misalignment. We therefore processed the later datasets (November 24) first as they contained full coverage of all GCPs. We then identified fixed objects that did not change during the study period (e.g., corner of a roof on a house, road markings). The 3-Dimensional coordinates from these manual tie points were then used on the earlier datasets to increase the geolocation accuracy and better align all datasets. The flow perimeter was manually digitized in ArcGIS and the resulting shapefile used as a mask to clip the raw point clouds to only the lava flow boundary and the surrounding topography. The point cloud was then classified into lava and vegetation that remained on top of the flow. Vegetation was filtered to remove any potential sources of false changes between dates. Each of the final point clouds were then converted into a 0.3 m DEM. The bare-earth elevation models were used to measure changes between datasets and to calculate total volume and area. In addition to the DEMs, a series of very high resolution (0.05 m) orthoimages were generated from Pix4D. The orthoimages were used to

identify morphological changes, track lateral and surface breakouts, and measure crack widths (Figure 3.2).

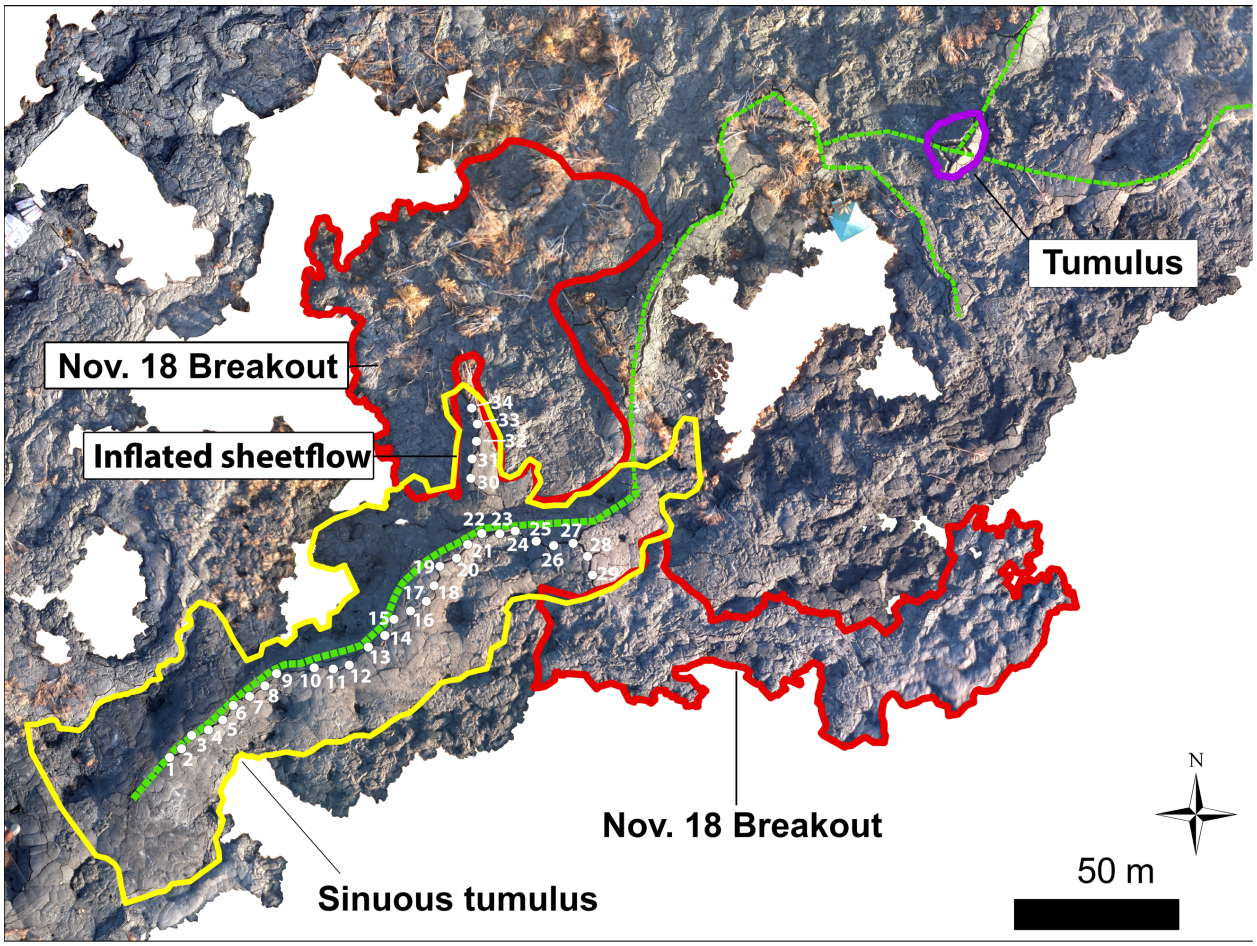

Figure 3.2. Map showing sinuous tumulus (yellow), crack measurements locations along sinuous tumulus (Table 2; white numbered points), November 18 breakouts (highlighted in dark red), tube system (dashed green lines), and a specific tumulus feature (purple) described in the text.

3.3 Results

3.3.1 General findings

While the flow front remained stalled through November, magma supply to the study region was maintained until November 18, and the flow experienced vigorous activity in the form of rapid inflation, and numerous lateral and minor surface breakouts, increasing the total area by 82,722 m^2 and total volume by 1,901,156 m^3 during a 4-week period. Surface inflation accounted for 56.5% of the new volume during this period (1,075,028 m^3). This was followed by lateral breakouts which accounted for 42.1% of volume (800,164 m^3) with the remainder (1.4%) due to

surface breakouts on top of the existing flow. The rate of magma supply averaged over the entire period was 0.9 m^3/s, very similar to the estimate of effusion rate of 1-2 m^3/s for the entire flow by Poland et al., (2016).

The data from the repeat surveys offers a more detailed picture (Figure 3.3). The total volume for the study region increased steadily at a rate of 1.2 m^3/s until November 18 when it slowed abruptly to 0.1 m^3/s. Initially the new mass was partitioned more or less evenly between inflation and lateral breakouts. However, from about November 11 until the end of activity, inflation played an increasingly significant role in terms of accommodating most of the new lava. New breakouts were insignificant after November 18 and the reduced mass flux was accommodated entirely as inflation.

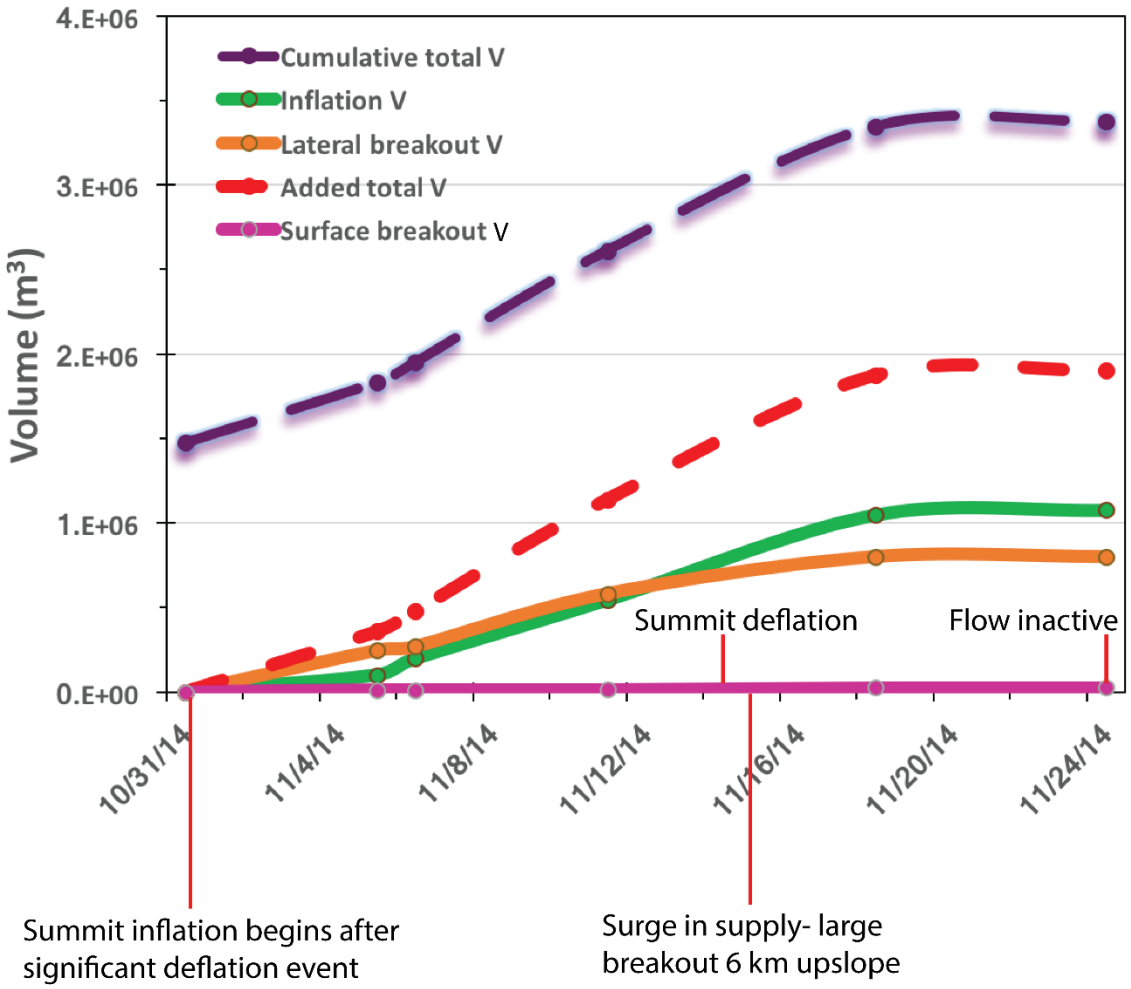

Figure 3.3 Plot showing cumulative total volume (m^3) over time which accounts for the pre-existing volume of the already emplaced flow from Oct. 31 (dashed purple line). Volume was partitioned by lateral breakouts (orange solid line), flow inflation (green solid line), surface breakouts (magenta solid line). The added total volume (dashed red line) represents new volume added to the flow during the study period ignoring the pre-existing volume already emplaced.

A central aim of this study was to assess the feasibility of quantifying critical parameters influencing lava flow dynamics across a stalled flow front. The DEM products derived from Structure-from-Motion software provided quantitative assessments of inflation, growth rates, volume, and area. We present three features of the evolving flow front that were readily quantified by UAS. These are:

1) Growth of an active tumulus on November 6 using detailed ground survey data in conjunction with UAS flights during a 9-hour survey period.

2) Development of a large active sinuous tumulus and the main feeder tube from Cemetery Rd. to the Pāhoa Japanese Cemetery.
3) Expansion behind the flow front following its stagnation from October 31 through November 24. This included partitioning between lateral breakouts, surface breakouts, and overall flow inflation.

3.3.2 Rise of a tumulus

We conducted simultaneous ground-surveys across an active tumulus that showed signs of vigorous activity (e.g., active surface breakouts, expanding surface cracks). Results from the survey, which was conducted on November 6, (Figure 3.4) show the high degree of agreement between the ground-surveys and Structure-from-Motion derived DEMs with an R^2 value of 0.9922 (Inset plot for flight 1, Figure 3.4). Flight 1 produced the poorest quality data of all datasets that day due to heavy smoke interference from nearby burning vegetation. The crest of the tumulus rose at an average rate of 0.16 m/hr over a 9-hour period, and showed a total inflation of >0.5 m based on DEM and GPS recordings. By November 11, the tumulus had inflated by an additional 1.8 m in elevation. The tumulus reached full maturity by November 18 during a surge in lava supply (we discuss details below), with a final gain of 0.6 m. In total, the tumulus inflated by 4.3 m between October 31, 2014, and November 24, 2014.

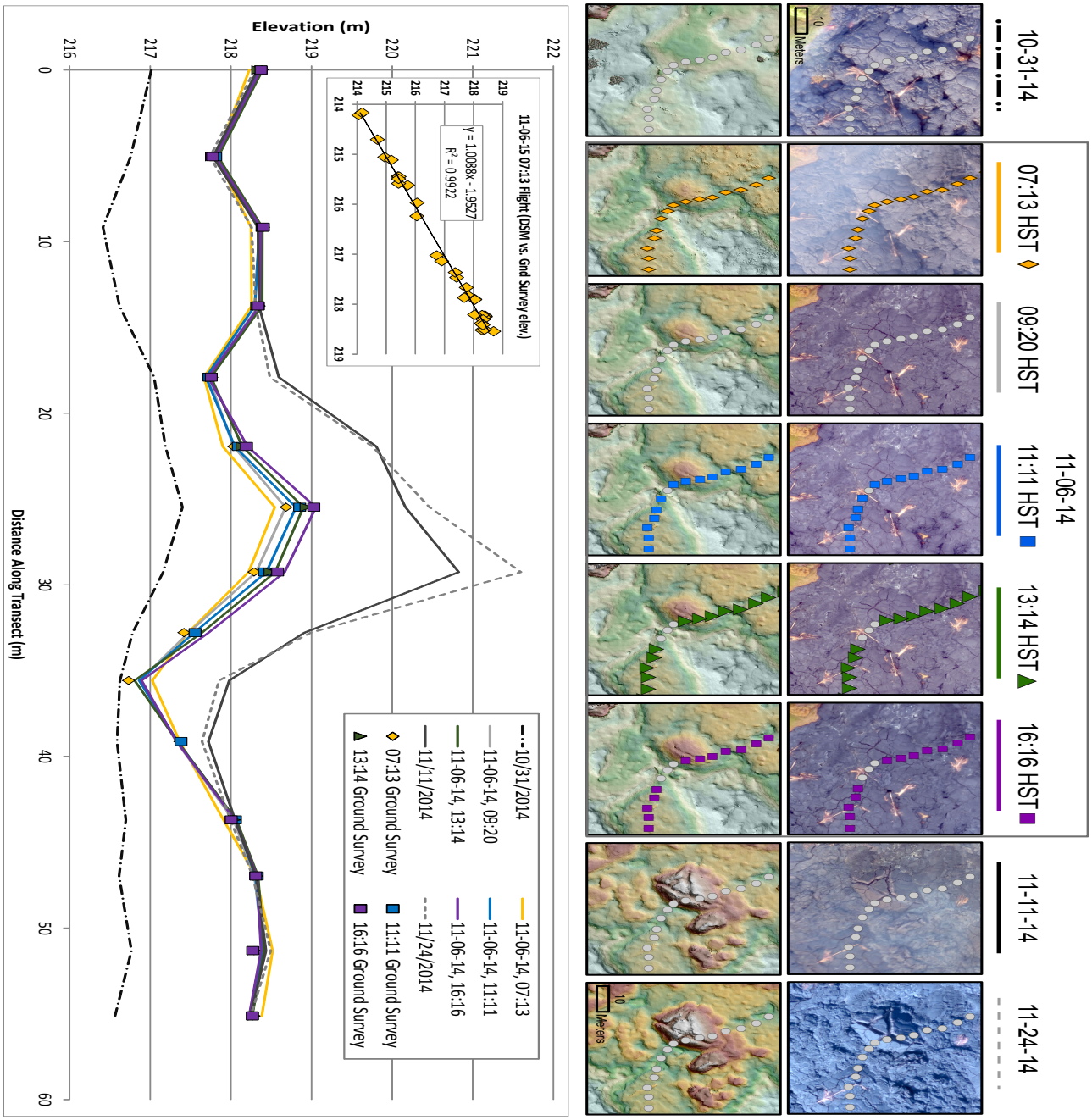

Figure 3.4 Assessment of UAS DEM quality comparing November 6 ground surveys with UAS DEMs. Five UAS flights (solid color lines) were conducted on November 6 starting at 07:13 HST with 2 hour intervals between flights. Simultaneous ground survey transects (diamond, triangle, and square symbols) were conducted over the tumulus with total station and RTK GPS. Also shown are the October 31 UAS DEM (dashed black line), November 11 UAS DEM (solid black

line), and November 24 UAS DEM (grey dashed line). Top panels show orthoimage for each datasets and corresponding shaded relief map based on DEM elevations. Inset plot shows UAS DEM vs ground survey DEM elevation values based on Flight 1 (07:13 HST) DEM. Transect is curved due to hazards that needed to be avoided by survey team.

3.3.3 Tube geometry

Accurate topographic measurements around the main feeder tube and subsequent distributary tubes were derived from step-wise calculations on a series of Structure-from-Motion generated DEMs from Cemetery Rd. to the tip of the stalled flow (Figure 3.1). Between October 31 and November 5th, the lava tube roof started to arch up in response to flow inflation. By November 11, a thick >3 m sinuous tumulus had formed above the main feeder tube, stopping short of the cemetery (Figure 3.2). The flow split and encircled the cemetery, but only developed a tube network on the left margin of the cemetery which created a bend as the tube curved around the cemetery (Figure 3.1). Traveling downslope after the cemetery we saw a steady decrease in total thickness of the overall geometry of the feeder tubes. The single feeder tube system devolved into a network of several branching distributary pathways. Growth of the distributary tubes in the study region appears to have ceased by November 6 and in some areas deflation occurred (Figure 3.5, segments 4, 5). The overall majority of growth due to inflation only occurred along the main feeder tube throughout the period (Figure 3.5, segment 2) while growth in other areas was due to a combination of inflation and breakouts.

3.3.4 Stress cracks along sinuous tumulus

The rapid growth of the sinuous tumulus was accompanied by stress cracks along the main axis of the tumulus. This eventually spread to the lateral sides of the tumulus highlighted in Figure 3.2. The width of dominant cracks on or near the crest of the sinuous tumulus were measured through time, using the rectified orthoimagery and are shown in Table 2 Appendix B. The main axial crack widened 2 m with the average crack length and width reaching 34 m and 1 m respectively after activity had ceased along the flow. Cracks above the tube and lateral margins of the tube widened up to 0.5 m in some locations. Lateral and surface breakouts occurred along the main tube and smaller distributary tubes downslope. Major cracks along the sinuous tumulus were also found to have shifted by several meters between November 11 and November 18 followed by significant widening during inflation.

Near the downstream end of the sinuous tumulus we observed the lateral breakout of a sheet flow that would later inflate and form an extension of the original sinuous tumulus. Inflation cracks along this solidified sheet flow (Point ID 30-34) were measured along with cracks along the adjacent head of the sinuous tumulus (Point ID 25-29). These two sections of the sinuous tumulus experienced rapid inflation (>2-3 m) between November 5 and November 11 (Figure 3.6, segment 2). The stress cracks measured at these locations widened by an average of 1.1 m (Table 2 Appendix B) significantly larger than the average of the other cracks along the sinuous tumulus (0.49 m). Within days of the November 17 surge the increased supply overwhelmed the (sinuous tumulus) with uplift of >1 m and shifted stress cracks by several meters along the mid-section of the sinuous tumulus. The simultaneous lateral breakouts occurred on both sides of the tube releasing ~26,000 m^3 of lava. These dual breakouts were short-lived and quickly solidified within a day.

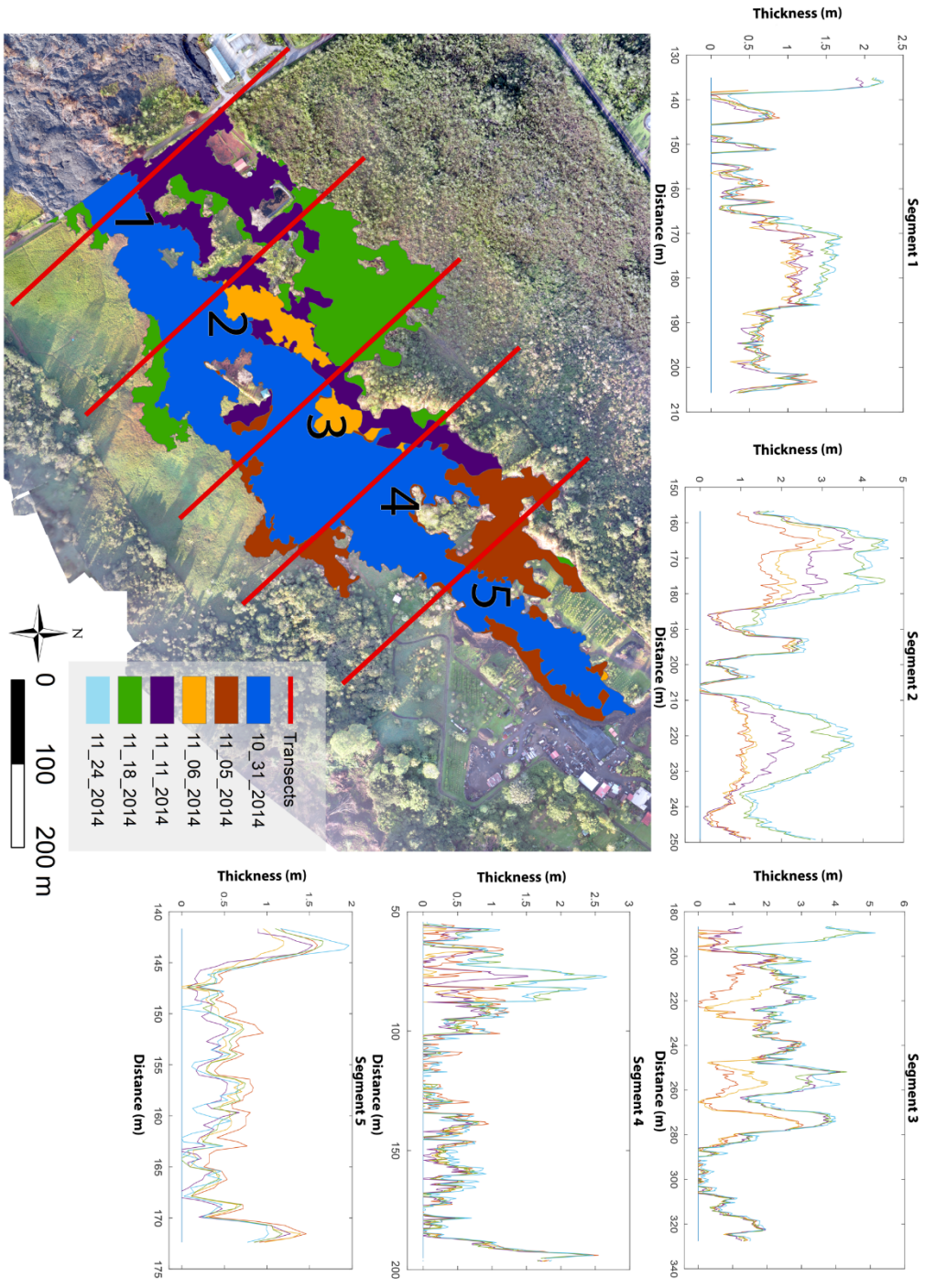

Figure 3.5. Digital transects (red lines) across the study region showing a time-series of elevation change at each segment. Oct. 31 was used as the baseline (blue) dataset from which to compare changes to Nov. 5 (brown), Nov. 6 (orange), Nov. 11 (purple), Nov. 18 (green), and Nov. 24 (teal) DEMs. Flow footprints based on the same corresponding color scheme are shown for the study site (starting at Cemetery Rd.) with an orthomosaic (Nov. 24) base map.

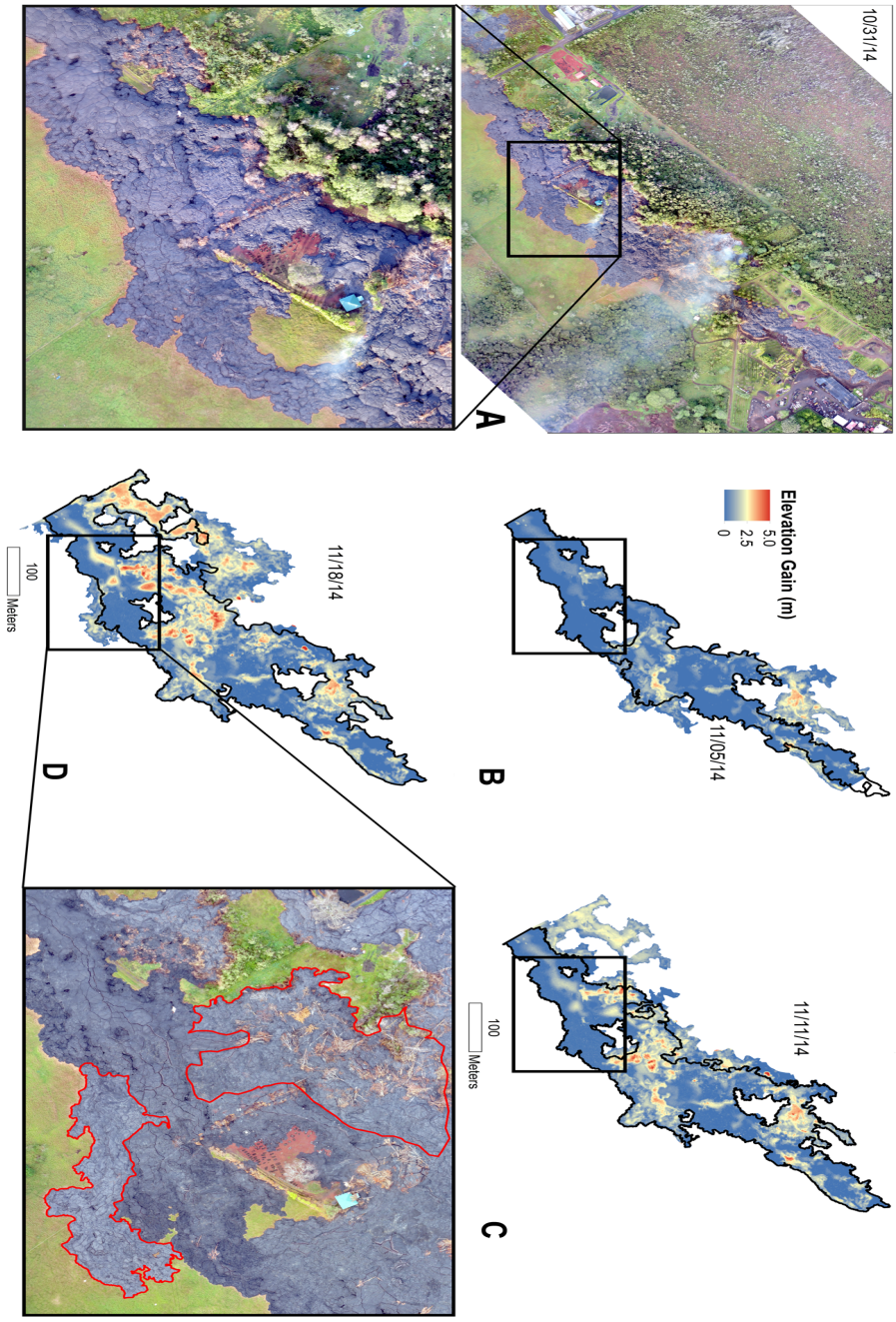

Figure 3.6. Time series documenting the Nov. 17 surge-triggered lateral breakouts. **A** Orthoimagery from Oct. 31, showing pre-breakout lava flow. **B** Inflation difference between Nov. 5, DEM and Oct. 31. DEM. **C** Inflation difference between Nov. 11 and Oct. 31 with Nov. 5 flow

margin outlined in black. **D** Inflation difference between Nov. 18 and Oct. 31 Box indicates area of orthoimagery showing surge triggered-breakouts (outlined in red).

3.3.5 Active inflation in the study region

Between October 31, 2014, and November 24, 2014, we mapped the study region 11 times. Over a series of 4 days beginning on Oct. 31 rapid inflation added 357,908 m^3 of new volume across the flow (Figure 3.3). Until November 11 lateral breakouts accounted for a larger share of new volume across the flow field. While inflation continued, some of the supply was diverted by lateral and surface breakouts, which increased in frequency and peaked by November 11 (Figure 3.7). On November 17, a large summit deflation/inflation event (Patrick et al. 2016) sent a surge of supply through the system. The surge was manifested in the study area by multiple lateral and surface breakouts in the study region (Figure 3.5), but most of the new volume was accommodated by inflation. All breakouts ceased within a day after the surge, but inflation continued to add new volume to the flow until ~November 24. Morphologically the majority of inflation was concentrated along the roof of the main feeder tube from the sinuous tumulus to surrounding area of the cemetery and to a lesser extent in areas that had recently formed as lateral breakouts from the tube system.

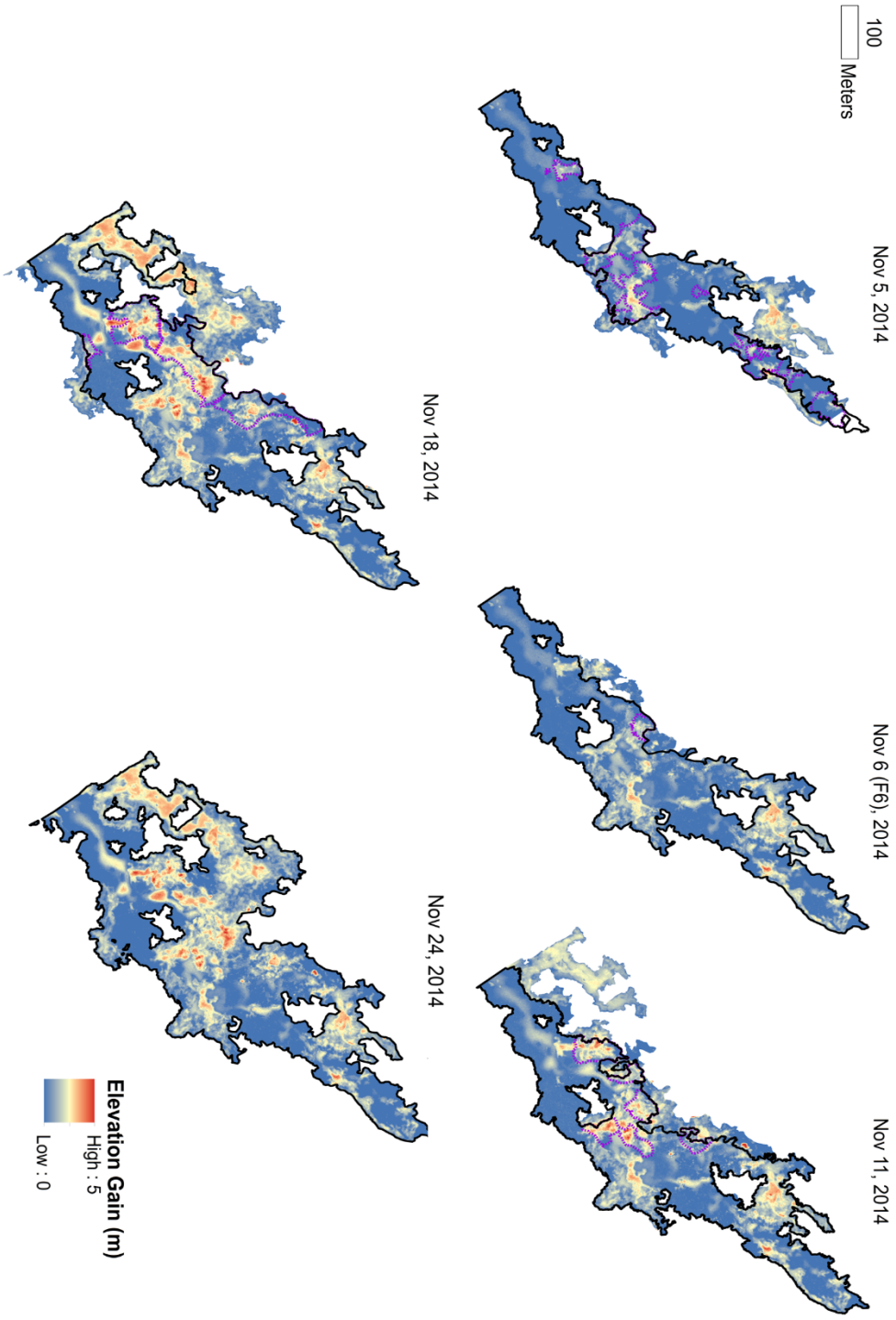

Figure 3.7 Cumulative inflation derived from a DEM subtraction between each consecutive dateset (Nov. 5, Nov. 6, Nov. 11, Nov. 18, Nov. 24) to the October 31 dataset (baseline). Red areas show up to 5 m of cumulative inflation, yellow (~2.5 m), and blue areas show no change in DEM

elevation. Black outlines show the flow outline from previous time step. Surface breakouts (non-inflation) are highlighted in purple dashed lines to exclude non-inflation related elevation gain. See Fig. 3.1 for location.

3.4 Discussion

3.4.1 Implications for active lava tube development

Pāhoehoe flows are capable of developing stable, well insulated tube systems enabling fresh lava to be delivered kilometers down range from the source vent, which are critical to long-lived flows (Mattox et al. 1993; Kauahikaua et al. 1998; Self et al. 1998). However, factors governing the rate and location of inflation over these preferred pathways are not well understood and particularly in regard to tube blockages and subsequent lateral breakouts along the margins of the system. Several studies have examined in detail pāhoehoe flow behavior as well as development of active tube systems, often at the scale of single tumuli (Hon et al. 1994) or small breakouts and cm-size lobes (Crown and Baloga 1999; Hamilton et al. 2013; Orr et al. 2015). However, the non-homogeneous rheology of pāhoehoe flows, which reflect such aspects as changing levels of supply, changes in the internal geometry of distributary tubes, local storage of supply and the influence of local changes in slope and roughness, make these detailed small-scale insights difficult to apply across larger-scale flow behavior. Previous studies that focused on lava tube development often describe the well-known roofing-over of flowing lava channels (James et al. 2012). In our case, the active development of a tube network was entirely due to inflation and internal storage of supply behind a stationary flow front. The stalled flow experienced less inflation than the regions proximal to the main feeder tubes where more local storage capacity existed. After the first week of our study we observed a shift in breakouts on the left margins of the flow specifically in areas that would later experience the greatest elevation gains due to inflation. Pre-flow topography played an influential role in determining where the preferred pathways were to form and subsequently where internal supply would build up before channeling into a lateral breakout. The Pāhoa Japanese Cemetery (Figure 3.1) in particular served as a local topographic high that split the flow in two, with the NW portion of the flow continuing to develop stable mature lava tubes while the SE portion of the flow ceased inflation and breakout activity. The initial flow morphology was predominantly that of a sheet flow with smooth and flat surfaces, which changed to a rough and uneven hummocky surface below the split at the cemetery. The initial sheet flow

developed into the sinuous tumulus (Figure 3.2) while the hummocky flow remained dominantly as hummocky pāhoehoe with inflation adding high ridges, tumuli and lava rises (Walker 1991).

3.4.2 Summit DI events and influence on flow activity

The Hawaiian Volcano Observatory relies on a network of summit tiltmeters stationed across both Halemaʻumaʻu and Puʻu ʻŌʻō vents to detect subsurface movement of magma. Cycles of deflation and inflation events (DI events) have been documented and known to cause variations in discharge from the source vent at Puʻu ʻŌʻō (Anderson K., Poland M., Johnson J. 2015; Orr et al. 2015). These DI events can switch rapidly between deflation/inflation within days, but visible influences on flow behavior down-channel of the source vent (manifested in the form of breakouts) can be delayed by several days after a DI event. Major switches from deflation to inflation can sometimes add a surge of supply into the upper system as the magma reservoir recovers. The June 27th flow advance continued until stalling on October 30, 2014. During the days prior to the flow front stalling, the tiltmeter network recorded a major summit deflation event which likely reduced the overall eruption rate and halted advance of the flow. By October 31 (the start of our study period) tiltmeters had recorded the summit returning to inflation. This inflation period continue throughout most of our study, associated with frequent lateral breakouts that expanded the overall area of the flow field. On November 17, the tiltmeter network recorded an abrupt switch from summit inflation to deflation. This coincided with a surge in lava supply into the lava system from the source vent within 24 hours. This surge triggered a breakout 6 km upslope of the stalled flow front. This large breakout on the left margin of the flow followed a new path of steepest descent, towards Pāhoa Marketplace. This breakout would go on to form its own insulated tube system and seal off the original tube system robbing all supply from the original flow lobe and resulting in its demise. Following the surge-triggered breakout upslope, short-lived lateral breakouts occurred along the sinuous tumulus (main tube system) before solidifying within the same day. However, inflation continued for at least a few more additional days, adding 27,942 m^3 of lava to the study region. By November 24, all supply to our study area had ceased. This event highlights the importance of surge-triggered breakouts induced by DI events at the summit, especially from a hazards context as the danger posed by the active flow front was shifted upslope and away from nearby communities. On March 9, 2015, ~17 weeks later, a massive surge-triggered breakout near the source vent at Puʻu ʻŌʻō (~15 km upslope) would halt and starve the new flow front, eliminating the threat posed by the June 27th flow to nearby communities in Puna.

3.4.3 Potential precursors to breakouts

The feeder tubes for pāhoehoe flows are notoriously leaky (Rossi and Gudmundsson 1996; Orr et al. 2015; Poland et al. 2016), but in a hazards context this behavior is critically important to improve breakout forecasts during an ongoing crisis. The tube system for this section of the flow has been characterized as experiencing major inflation along the main tube corridor before transitioning into a network of smaller distributary tubes as it curved around the cemetery. Using the October 31 DEM as the baseline topography (Figure 3.5), the sinuous tumulus section of the tube experienced rapid inflation on the order of 1-3 m within the first week and a peak of 3.8 m within 11 days. This section of the tube system seems to have been absorbing large quantities of the increasing supply of fresh lava. A series of axial stress fractures along the sinuous tumulus began to form shortly after October 31. For the first 11 days, these cracks were stationary and widened by < 1 m. Between November 11 and November 18 some of these cracks shifted by several cm during inflation and widened up to 2 m in some locations. These observations likely indicate a shift from a predominantly viscoelastic crust to a significant hardened, brittle crust especially after inflation induced thickening of the sinuous tumulus. We cannot say for certain that the underlying cause for this shift and widening of crack diameters was due to the DI surge-triggered event, but inflation in this area may have been required to accommodate the increased supply.

The sinuous tumulus displayed several key warning symptoms prior to the lateral breakouts (Figure 3.2) including a higher rate (2-3 m) of inflation during the first two weeks, stress cracks that widened by up to 1 m at crack stations 25-34 (Figure 3.2), and a sharp bend in lava tube geometry around the cemetery (Figure 3.1). From a hazard perspective, these early symptoms of inflation and visible fractures likely reflect changes in the internal geometry of a feeder tube as it changes in response to topographic confinement, internal blockages, and changes in supply rate entering the system. It also brings to light the importance of the internal geometry of the feeder tubes where sections of the tube that begin to diminish in size can become weak points in the system (Figure 3.5) and are prone to blockages and/or release of lateral breakouts during surge-trigged events. Early identification of such changes in tube geometry could help monitoring scientists pinpoint likely breakout locations (Figure 3.1). If inflation and morphological changes are monitored consistently across the flow field, scientists might one day be able to forecast the

precise locations and timing of subsequent major breakouts along the system as they are forewarned by DI events at the summit.

3.5 Conclusions

We used aerial imagery collected by UAS to quantify aspects of inflation, formation of tumuli, and breakouts behind the stalled front of a pāhoehoe lava flow during the 2014-2015 Pāhoa lava flow crisis. Highlights from this study include:

(1) Quantifying the competing processes of flow inflation (56.5%), surface breakouts (1.4%) and lateral breakouts (42.1%) in accommodating new magma entering the study region.
(2) The development of a sinuous tumulus over a lava tube system entirely derived from inflation was captured during a relatively short period (4-weeks).
(3) Repeated step-wise measurements of inflation, stress cracks, and growth rates show precursors to breakouts that may provide better estimates of future flow behavior and help to reduce the uncertainty in hazard forecasts.

UAS studies are a powerful new tool for understanding fundamental processes of advance and evolution of pāhoehoe lava flows. Equally critically, if the primary goal of active volcano monitoring is to provide accurate and timely forecasts of future flow activity, UAS can provide valuable insights into changing flow behavior by showing where active inflation occurs, and formation of stress fractures, tumulus, and subsequent breakouts. UAS can complement existing techniques employed by volcano observatories and provide more detailed inputs for developing better lava flow forecast models geared towards pāhoehoe flows.

Table 1 Appendix A.

Flight No.	Number of photos collected	GCPs Used (Name)	Number of GCPs	Date of Flight
1	270	2,3,4,5,6,7,8,9	8	Dec 16, 2014
2	293	1,2,3,4,5,6,7,8,16,17,18	11	Dec 17, 2014
3 + 4	589	10,11,12,13,14,15	6	Jan 8, 2015
5	244	6,7,8,9	4	Jan 8, 2015
6	250	8,10,19,20,21,22	6	Jan 19, 2015
7	145	8,10,14,15	4	Jan 19,2015
8	272	10,11,12,13,14,15	6	March 19, 2015
9	179	7,8,10	3	March 19, 2015
10	183	1,2,3,4,5,6,7,9	8	March 19, 2015
11	194	23,24,25,26,27,28,29,30	8	March 24, 2016
12	158	32,38,39,40,41,42,48,49	8	March 24, 2016
13	266	31,33,34,36,37,38,	6	March 24, 2016
14	259	30,31,33,34,35	5	March 24, 2016
15	221	35,43,44,45	4	March 25, 2016
16	221	43,44,45,46	4	March 25, 2016
17	189	43,46,47	3	March 25, 2016
18	255	36,43,46,47	4	March 25, 2016
19	201	27,32,41	3	May 2, 2016
20	257	26,27,28,32	4	May 2, 2016
21	321	26,27,28,29,32	5	July 26, 2016
22+23	614	37,38,39,40,41,42,48,47	8	July 26, 2016

Table 2 Appendix B.

Date	ID	Crack Width (m)	Tumulus height (m)	Tumulus width (m)	Tumulus Aspect ratio
11/24/2014	1	0.64	2.4	47.2	0.05
11/24/2014	2	0.62	2.1	40.7	0.05
11/24/2014	3	0.64	2.3	37.3	0.06
11/24/2014	4	0.76	2.1	33.8	0.06
11/24/2014	5	0.62	2.4	36.9	0.06
11/24/2014	6	0.58	2.4	46.4	0.05
11/24/2014	7	0.71	2.4	52.2	0.05
11/24/2014	8	0.40	2.1	33.7	0.06
11/24/2014	9	0.32	2.1	33.5	0.06
11/24/2014	10	0.83	2.8	35.3	0.08
11/24/2014	11	0.70	3.5	40.0	0.09
11/24/2014	12	0.68	3.5	35.2	0.10
11/24/2014	13	1.05	3.5	39.1	0.09
11/24/2014	14	0.71	3.3	38.5	0.09
11/24/2014	15	0.68	4.1	60.0	0.07
11/24/2014	16	0.76	4.4	60.7	0.07
11/24/2014	17	0.74	4.4	59.7	0.07
11/24/2014	18	0.97	4.0	58.2	0.07
11/24/2014	19	1.12	5.0	57.1	0.09
11/24/2014	20	1.17	5.0	54.3	0.09
11/24/2014	21	0.73	3.1	42.1	0.07
11/24/2014	22	1.66	3.5	40.3	0.09
11/24/2014	23	1.66	3.0	48.0	0.06
11/24/2014	24	1.84	3.0	58.5	0.05
11/24/2014	25	1.05	3.4	73.3	0.05
11/24/2014	26	1.80	3.4	33.5	0.10
11/24/2014	27	1.61	4.9	29.5	0.17
11/24/2014	28	1.02	4.9	30.0	0.16
11/24/2014	29	0.88	4.6	30.0	0.15
11/24/2014	30	1.65	4.6	30.0	0.15
11/24/2014	31	1.31	4.9	48.0	0.10
11/24/2014	32	1.26	3.9	58.5	0.07
11/24/2014	33	1.61	3.9	73.3	0.05
11/24/2014	34	1.36	4.9	73.3	0.07

11/18/2014	1	0.34	1.9	47.2	0.04
11/18/2014	2	0.47	1.6	40.7	0.04
11/18/2014	3	0.35	2.3	37.3	0.06
11/18/2014	4	0.52	2.1	33.8	0.06
11/18/2014	5	0.43	2.4	36.9	0.07
11/18/2014	6	0.46	2.6	46.4	0.06
11/18/2014	7	0.44	1.7	52.2	0.03
11/18/2014	8	0.30	1.7	33.7	0.05
11/18/2014	9	0.31	1.7	33.5	0.05
11/18/2014	10	0.69	2.6	35.3	0.07
11/18/2014	11	0.48	2.7	40.0	0.07
11/18/2014	12	0.43	2.7	35.2	0.08
11/18/2014	13	0.94	2.5	39.1	0.06
11/18/2014	14	0.44	3.0	38.5	0.08
11/18/2014	15	0.44	3.0	60.0	0.05
11/18/2014	16	0.50	3.0	60.7	0.05
11/18/2014	17	0.49	2.7	59.7	0.05
11/18/2014	18	0.61	2.8	58.2	0.05
11/18/2014	19	0.63	2.7	57.1	0.05
11/18/2014	20	0.49	2.4	54.3	0.04
11/18/2014	21	0.56	2.0	42.1	0.05
11/18/2014	22	1.18	1.8	40.3	0.05
11/18/2014	23	0.92	1.8	48.0	0.04
11/18/2014	24	1.26	1.8	58.5	0.03
11/18/2014	25	0.79	1.9	73.3	0.03
11/18/2014	26	1.05	3.2	33.5	0.10
11/18/2014	27	1.53	3.9	29.5	0.13
11/18/2014	28	0.76	3.7	30.0	0.12
11/18/2014	29	0.50	2.5	30.0	0.08
11/18/2014	30	0.92	4.5	30.0	0.15
11/18/2014	31	0.69	3.9	48.0	0.08
11/18/2014	32	0.75	3.9	58.5	0.07
11/18/2014	33	0.71	3.9	73.3	0.05
11/18/2014	34	0.80	4.2	73.3	0.06
11/11/2014	1	0.32	1.2	47.2	0.03
11/11/2014	2	0.37	1.2	40.7	0.03
11/11/2014	3	0.24	1.4	37.3	0.04
11/11/2014	4	0.26	1.1	33.8	0.03
11/11/2014	5	0.18	1.3	36.9	0.03
11/11/2014	6	0.40	1.2	46.4	0.02
11/11/2014	7	0.25	1.2	52.2	0.02

11/11/2014	8	0.13	1.2	33.7	0.03
11/11/2014	9	0.24	1.0	33.5	0.03
11/11/2014	10	0.69	1.5	35.3	0.04
11/11/2014	11	0.54	1.4	40.0	0.03
11/11/2014	12	0.22	1.4	35.2	0.04
11/11/2014	13	0.40	1.5	39.1	0.04
11/11/2014	14	0.38	2.1	38.5	0.05
11/11/2014	15	0.22	1.9	60.0	0.03
11/11/2014	16	0.20	2.1	60.7	0.03
11/11/2014	17	0.24	1.7	59.7	0.03
11/11/2014	18	0.27	1.9	58.2	0.03
11/11/2014	19	0.31	2.0	57.1	0.04
11/11/2014	20	0.49	1.7	54.3	0.03
11/11/2014	21	0.31	1.5	42.1	0.03
11/11/2014	22	0.62	1.4	40.3	0.04
11/11/2014	23	0.89	1.3	48.0	0.03
11/11/2014	24	0.83	1.6	58.5	0.03
11/11/2014	25	0.41	1.4	73.3	0.02
11/11/2014	26	0.38	2.1	33.5	0.06
11/11/2014	27	0.37	2.2	29.5	0.07
11/11/2014	28	0.32	2.0	30.0	0.07
11/11/2014	29	0.42	1.3	30.0	0.04
11/11/2014	30	0.28	3.6	30.0	0.12
11/11/2014	31	0.40	2.7	48.0	0.06
11/11/2014	32	0.44	3.1	58.5	0.05
11/11/2014	33	0.61	3.0	73.3	0.04
11/11/2014	34	0.61	3.0	73.3	0.04
11/6/2014	1	0.29	1.2	47.2	0.03
11/6/2014	2	0.31	0.8	40.7	0.02
11/6/2014	3	0.23	1.1	37.3	0.03
11/6/2014	4	0.24	1.1	33.8	0.03
11/6/2014	5	0.18	0.9	36.9	0.03
11/6/2014	6	0.40	0.9	46.4	0.02
11/6/2014	7	0.25	0.7	52.2	0.01
11/6/2014	8	0.13	1.1	33.7	0.03
11/6/2014	9	0.25	0.9	33.5	0.03
11/6/2014	10	0.46	0.9	35.3	0.03
11/6/2014	11	0.39	1.3	40.0	0.03
11/6/2014	12	0.23	1.1	35.2	0.03
11/6/2014	13	0.40	0.9	39.1	0.02
11/6/2014	14	0.38	1.1	38.5	0.03
11/6/2014	15	0.23	1.3	60.0	0.02

11/6/2014	16	0.21	1.2	60.7	0.02
11/6/2014	17	0.25	1.1	59.7	0.02
11/6/2014	18	0.27	1.3	58.2	0.02
11/6/2014	19	0.31	1.2	57.1	0.02
11/6/2014	20	0.50	1.3	54.3	0.02
11/6/2014	21	0.32	1.2	42.1	0.03
11/6/2014	22	0.64	1.2	40.3	0.03
11/6/2014	23	0.89	1.0	48.0	0.02
11/6/2014	24	0.85	1.2	58.5	0.02
11/6/2014	25	0.06	0.7	73.3	0.01
11/6/2014	26	0.32	1.3	33.5	0.04
11/6/2014	27	0.39	1.2	29.5	0.04
11/6/2014	28	0.28	1.2	30.0	0.04
11/6/2014	29	0.10	1.0	30.0	0.03
11/6/2014	30	0.24	3.0	30.0	0.10
11/6/2014	31	0.13	2.1	48.0	0.04
11/6/2014	32	0.30	2.3	58.5	0.04
11/6/2014	33	0.28	2.5	73.3	0.03
11/6/2014	34	0.40	1.9	73.3	0.03
11/5/2014	1	0.28	1.0	47.2	0.02
11/5/2014	2	0.28	1.0	40.7	0.02
11/5/2014	3	0.00	1.3	37.3	0.03
11/5/2014	4	0.19	1.1	33.8	0.03
11/5/2014	5	0.11	1.0	36.9	0.03
11/5/2014	6	0.30	1.0	46.4	0.02
11/5/2014	7	0.21	1.0	52.2	0.02
11/5/2014	8	0.00	1.2	33.7	0.04
11/5/2014	9	0.22	1.3	33.5	0.04
11/5/2014	10	0.42	1.0	35.3	0.03
11/5/2014	11	0.37	1.3	40.0	0.03
11/5/2014	12	0.22	1.2	35.2	0.03
11/5/2014	13	0.37	0.81	39.1	0.02
11/5/2014	14	0.37	1.1	38.5	0.03
11/5/2014	15	0.21	1.2	60.0	0.02
11/5/2014	16	0.21	1.2	60.7	0.02
11/5/2014	17	0.24	1.2	59.7	0.02
11/5/2014	18	0.27	1.1	58.2	0.02
11/5/2014	19	0.30	1.2	57.1	0.02
11/5/2014	20	0.49	1.4	54.3	0.03
11/5/2014	21	0.30	1.4	42.1	0.03
11/5/2014	22	0.63	1.1	40.3	0.03
11/5/2014	23	0.88	1.1	48.0	0.02

11/5/2014	24	0.83	1.0	58.5	0.02
11/5/2014	25	0.00	0.7	73.3	0.01
11/5/2014	26	0.21	1.0	33.5	0.03
11/5/2014	27	0.27	1.1	29.5	0.04
11/5/2014	28	0.23	1.0	30.0	0.03
11/5/2014	29	0.11	0.9	30.0	0.03
11/5/2014	30	0.00	2.8	30.0	0.09
11/5/2014	31	0.00	1.7	48.0	0.04
11/5/2014	32	0.09	1.8	58.5	0.03
11/5/2014	33	0.00	1.9	73.3	0.03
11/5/2014	34	0.00	1.5	73.3	0.02

Chapter 4

Final Conclusions

4.1 The role of unmanned aerial systems in volcanology

Kīlauea Volcano and her sister volcano Mauna Loa are two of the world's most active volcanoes with high potential to produce basaltic lava flows that threaten nearby communities on the Island of Hawai'i in the near future. The emplacement of the recent June 27th lava flow highlighted important gaps in knowledge within the volcanology community as to how low-effusion rate pāhoehoe lava flows evolve even during periods of little to no flow advancement. The June 27th flow also revealed challenges faced by monitoring scientists and emergency officials in anticipating future flow activity and keeping the public supplied with up to date information on the flows' status. From a hazards perspective, the underlying challenge is the amount of uncertainty in what the flow is currently doing and what it might do in the short-term. To adequately meet this challenge constant streams of new information are needed. The data need to be reliable, consistent, cost-effective, and spatially and temporally relevant.

Unmanned aerial systems can support scientists in meeting this challenge through repeated surveys with low operational costs (e.g., low-cost hardware, no aviation fuel costs, no data costs) and provide a means to collect consistent data with low-risk to human life (e.g., low-altitude flights are high-risk for all manned aircraft). More importantly UAS can support all monitoring phases of an active lava flow from generating updated paths of steepest descent during flow advancement to monitoring the evolution of key processes across an entire flow field in the hopes of predicting potential breakout locations using precursors of inflation, extensional fractures, and the geometry of the tube system(s). During the Pāhoa crisis, in 2014, Civil Defense officials at one point requested 24/7 monitoring around the perimeter of the flow front as it approached nearby homes. Many residents did not want to evacuate unless absolutely needed to and preferred to stay in residence until the flow was a visible threat. Science agencies often lack the workforce to accommodate such requests, but could supplement their personnel, mapping with UAS flights day and night (thermal sensors would be required for night flights). In 2014, the FAA was very restrictive in terms of approving UAS flights in the National Airspace System. In 2016, the rules changed and the process has been streamlined to accommodate requests such as night flying and even beyond-line-of-sight

flights. The responsibility and liability for flight safety is now entirely on remote pilots and no longer tied to the organization they fly for. This will hopefully in turn encourage more risk-averse organizations to embrace UAS as a possible tool for their operations.

4.2 Research limitations

4.2.1 Chapter 2

UAS are not without their own limitations and challenges. The technology itself is still young and evolving in parallel with regulations that vary in countries around the world. Our biggest challenge during the 2014-2015 Pāhoa crisis was getting permission to fly in the first place. Whereas UH Hilo had existing Certificates of Authorization (COA) for some parts of the island of Hawai‘i, none were for the Puna district. Furthermore, we needed to acquire a COA within weeks, when at the time, the normal FAA process took 3 months to a year for approval. It took a special request to the director of the FAA for our COA to be approved by reassigning an already approved COA for the same UAS platform from a different location on the island. After securing approval from both the FAA and Hawaii Civil Defense, the next issue was keeping visible line-of-sight of the UAS at all times of flight as per FAA regulations. Our maiden flight on October 22, 2014, took place while the flow was still on the outskirts of Pāhoa and in dense foliage. A fire department helicopter tracked our UAS from the sky to maintain contact with the UAS at all times. The line-of-sight regulation, which is standard for all UAS in United States airspace, can be a major limitation for many science applications. Although exemptions can be requested to fly beyond line-of-sight, they are not always approved, especially in areas with high aircraft traffic. UAS technology is still in need of an automated air traffic control system to make long-distance flights safely feasible. Note that NASA and several tech companies are currently working on such systems, but none have been widely adopted at the time of writing. Other challenges during UAS flight operations included keeping in contact with nearby manned aircraft and dealing with changing weather (e.g., strong winds, rain, or smoke from burning vegetation). Weather effects interfered with optical sensors sometimes causing blurry images which either render the data unusable or reduce the accuracy of Structure-from-Motion derived models. They also pose a direct hazard to UAS, with many systems having a maximum wind speed capacity.

4.2.2 Chapter 3

The maiden flight of our study period on October 31, 2014, proved challenging as we needed to mark and survey ground control points (GCP) around the flow prior to flights. The pressure to fly before we lost our flight window for the day meant our baseline dataset lacked GCPs compared to later datasets. A limiting factor for high precision mapping then is properly deploying GCPs prior to any UAS flights. Some UAS systems offer Real-Time Kinematic (RTK) capability which can potentially reduce or eliminate the need for GCPs depending on the quality of the RTK base station used to send corrections to the UAS in-flight.

Another consideration during flights is to map at a similar time of day. This in theory will keep shadows consistent between images and reduce artificial noise in the dataset caused by shadows in one scene, but not the next. We tried to be as consistent as possible during flight operations and normally aimed for mid to late morning flights. If we saw a cloud passing over before launch, we might hold-off for a few minutes to keep lighting consistent. Although high noon is often the preferred time of day to minimize shadows from the sun this was not a practical time at our study site characterized by frequent strong winds in the afternoon that would bring with them passing showers. The weather dynamics around Pāhoa are difficult to predict and always changing.

4.3 Future Research

4.3.1 Additional Sensor Payloads

UAS are still considered an emerging technology, one that has not yet reached its full potential (Wendel 2017). Suitable sensors such as lidar scanners, thermal infrared and hyperspectral cameras are becoming smaller, lighter, and cheaper specifically for the growing UAS industry. Helicopter-borne thermal imagery has already been proven to capture temperature changes across a flow field and help delineate the active tube system (Patrick et al. 2016). A dual mounted payload using thermal and visible cameras could capture both types of data simultaneously providing the temperature benefits of thermal data with the higher spatial resolution 3D-dimensional models from the visible data. Whereas 3-Dimensional models can be generated from thermal imagery, their poor spatial resolution makes their resulting models inferior. The two data types can support each other and offer new insights into flow dynamics. This could be especially useful in detecting areas prone to breakouts as the combination of inflation, changes

in visible cracks, and the estimated crustal thickness based from thermal data would help locate areas prone to future breakouts along an active tube system. Visible imagery collected via helicopter might lack the required spatial resolution to locate stress cracks due to altitude limitations and challenges in the precision of flight paths. The addition of lidar could improve 3-Dimensional mapping of the either the lava flow itself or surrounding topography. Lidar especially excels in vegetated areas where canopy shadows block passive optical sensors from penetrating to the bare earth. The higher quality DEMs could be used for improved flow path forecasting. Hyperspectral sensors and mass spectrometers have been used to study gas plumes in detail (Diaz et al. 2015) and their use extended to collect ash samples as well during larger explosive eruptions.

4.3.2 Swarm Mapping

Flying multiple UAS simultaneously that are capable of communicating to each other and often controlled autonomously is known as swarm flying in robotics (Kim et al. 2017). A key challenge with mapping lava flows is the spatial area that must be covered if the entire flow is to be mapped. This is likely the greatest weakness of UAS at this time partly due to technology (e.g., most UAS platforms have short endurance < 1 hour) and partly due to current regulations (e.g., The FAA is very restrictive on allowing multiple UAS flights simultaneously and requires special approval). However, as more sophisticated air traffic management systems come online and the FAA regulations continue to evolve, multiple UAS operations will become a common occurrence. Tech companies (e.g., Intel, Amazon, Google, Precision Hawk) in addition to NASA have been working on SWARM technology ranging from drone delivery to aerial light shows as entertainment. Hundreds of UAS can be controlled by a single operator in real-time. An obvious extension of this technology would be to use multiple fixed-wing UAS to cover different sections of a lava flow simultaneously providing total coverage of the flow. This could increase the temporal coverage to capture rapidly changing features (e.g., advancing fronts of ‘a‘ā flows).

4.3.3 Machine Learning Applications

Machine learning allows a computer to learn from new data instead of being implicitly programmed to accomplish a task. Deep learning (a subfield of machine learning) uses layers of convolutional neural networks (CNN) to understand content from an image. This technology has enabled very accurate classifications of content and features within video or image datasets. A CNN agent could be trained to automatically classify specific features across a lava flow (tumuli,

axial cracks along tubes etc.,) using high resolution imagery collected via UAS. Imagery like that collected from the June 27th flow can be combined with imagery collected from other lava flows across the world forming a UAS lava flow repository. The repository would be used to train an agent, to be embedded into a software application for lava flow monitoring. The lava flow app could ingest real-time imagery during or shortly after a UAS flight, process the imagery with Structure-from-Motion in the cloud, and then automatically identify precursor symptoms to breakouts as new data came in with each flight. This level of automation would allow the June 27th scenario to play out much differently from a monitoring context, especially had the lava flow continued into populated areas of Pāhoa. Scientists would be alerted in real-time as the system identified new breakout threats and be provided a probability rating of risk in high-threat areas across the flow.

4.3.4 Remote Drone Ports

Multiple tech companies have been working on remote drone ports that can house, recharge, and launch UAS in remote areas. These systems are usually solar powered and can automatically upload data to the cloud after the UAS has landed. A drone port might be deployed around the summit of an active volcano and provide daily automated launches to map changes in morphology, take gas samples, and map temperature changes. These could be formed into a network of stations for full coverage across the volcano similar to the seismic, GPS, and web cam networks spread across Kilauea and Mauna Loa in Hawai‘i. A volcano observatory or even an academic research center might remotely monitor multiple active volcanoes with such a network. UAS are mobile and not restricted to a single location, unlike traditional web cameras, thus providing a quick response tool when signs of unrest appear.

4.3.5 UAS Platforms

The type of aircraft for a project can make a critical difference in reaching project goals. Fixed-wing UAS that are designed as airplanes feature longer-endurance, larger geographic coverage for mapping, and travel faster compared to multi-rotors. Our chosen platform for the lava flow project was a fixed-wing in part because of its longer endurance and capability to map a larger area. A major drawback to our choice was the requirement for a some type of runway to land. We were fortunate to take advantage of the pasture field surrounding the stalled flow front. When the second flow front later approached the Pahoa Marketplace, we had to land in a thick topical forest.

We took advantage of a bulldozed firebreak created to keep wildfires sparked by the the lava flow at bay and used it as our runway for landings. Multi-rotors provide flexibility by not requiring a large area for landing. They are also better equipped to fly at very low altitudes without as much risk from tail winds pushing the aircraft into the ground. Lower altitudes of course mean less geographic coverage. The limited flight times of common multi-rotors are often it's weakness compared to fixed-wing platforms. Hybrid UAS mix the two types of platforms and are often referred to as vertical take-off and landing (VTOL) UAS. The design of hybrids aim for the endurance of a fixed-wing, but the flexibility of a multi-rotor. Most hybrids can't fly as long as a traditional fixed-wing, but their VTOL capability make up for that short-coming for projects that do not require long-endurance flights.

References

Anderson K., Poland M., Johnson J. MA (2015) Episodic deflation-inflation events at Kīlauea Volcano and implications for the shallow magma system. Hawaiian Volcanism From Source to Surface, AGU Geophysical Monograph Series

Anderson SW, Smrekar SE, Stofan ER (2012) Tumulus development on lava flows: Insights from observations of active tumuli and analysis of formation models. Bull Volcanol 74:931–946 . doi: 10.1007/s00445-012-0576-2

Cashman K V., Soule SA, Mackey BH, et al (2013) How lava flows: New insights from applications of lidar technologies to lava flow studies. Geosphere 9:1664–1680 . doi: 10.1130/GES00706.1

Crown D a., Baloga SM (1999) Pāhoehoe toe dimensions, morphology, and branching relationships at Mauna Ulu, Kīlauea Volcano, Hawai'i. Bull Volcanol 61:288–305 . doi: 10.1007/s004450050298

Diaz JA, Pieri D, Wright K, et al (2015) Unmanned Aerial Mass Spectrometer Systems for In-Situ Volcanic Plume Analysis. 292–304 . doi: 10.1007/s13361-014-1058-x

Dietterich HR, Poland MP, Schmidt DA, et al (2012) Tracking lava flow emplacement on the east rift zone of Kīlauea, Hawaii, with synthetic aperture radar coherence. Geochemistry, Geophys Geosystems 13:1–17 . doi: 10.1029/2011GC004016

Hamilton CW, Glaze LS, James MR, Baloga SM (2013) Topographic and stochastic influences on pāhoehoe lava lobe emplacement. Bull Volcanol 75:1–16 . doi: 10.1007/s00445-013-0756-8

Harwin S, Lucieer A (2012) Assessing the accuracy of georeferenced point clouds produced via multi-view stereopsis from Unmanned Aerial Vehicle (UAV) imagery. Remote Sens 4:1573–1599 . doi: 10.3390/rs4061573

Hon K, Kauahikaua J, Denlinger R, Mackay K (1994) Emplacement and inflation of pāhoehoe sheet flows: observations and measurements of active lava flows on Kīlauea volcano, Hawaii. Geol Soc Am Bull 106:351–370 . doi: 10.1130/0016-7606(1994)106<0351:EAIOPS>2.3.CO;2

James MR, Applegarth LJ, Pinkerton H (2012) Lava channel roofing, overflows, breaches and switching: Insights from the 2008-2009 eruption of Mt. Etna. Bull Volcanol 74:107–117 . doi: 10.1007/s00445-011-0513-9

Kauahikaua, J., Mangan, M., Heliker, C., Mattox T (1996) A quantitative look at the demise of a basaltic vent: the death of Kupaianaha, Kīlauea Volcano, Hawai'i. Bull Volcanol 57:641–648

Kauahikaua J, Cashman K V., Mattox TN, et al (1998) Observations on basaltic lava streams in

tubes from Kīlauea Volcano, island of Hawai'i. J Geophys Res Solid Earth 103:27303–27323 . doi: 10.1029/97JB03576

Kauahikaua JP, Sherrod DR, Cashman K V, et al (2003) Hawaiian lava-flow dynamics during the Pu'u 'O'o-Kupaianaha eruption: a tale of two decades. US Geol Surv Prof Pap 1676 63–87

Kim HJ, Ahn HS (2017) Realization of swarm formation flying and optimal trajectory generation for multi-drone performance show. SII 2016 - 2016 IEEE/SICE Int Symp Syst Integr 850–855 . doi: 10.1109/SII.2016.7844106

Küng O, Strecha C, Beyeler A, et al (2011) The Accuracy of Automatic Photogrammetric Techniques on Ultra-Light UAV Imagery. ISPRS - Int Arch Photogramm Remote Sens Spat Inf Sci XXXVIII-1/:125–130 . doi: 10.5194/isprsarchives-XXXVIII-1-C22-125-2011

Macdonald GA (1953) Pāhoehoe, a'a, and block lava. Am. J. Sci. 251:169–191

Mattox TN, Heliker C, Kauahikaua J, Hon K (1993) Development of the 1990 Kalapana Flow Field, Kīlauea Volcano, Hawaii. Bull Volcanol 55:407–413 . doi: 10.1007/BF00302000

Orr TR, Bleacher JE, Patrick MR, Wooten KM (2015) A sinuous tumulus over an active lava tube at Kīlauea Volcano: Evolution, analogs, and hazard forecasts. J Volcanol Geotherm Res 291:35–48 . doi: 10.1016/j.jvolgeores.2014.12.002

Orr TR, Heliker C, Patrick MR (2013) The ongoing Pu'u 'O'o eruption of Kīlauea Volcano, Hawai'i—30 years of eruptive activity. US Geol Surv Fact Sheet 2012-3127 6 p.

Patrick M, Orr T, Fisher G, et al (2017) Thermal mapping of a pāhoehoe lava flow, Kīlauea Volcano. J Volcanol Geotherm Res 332:71–87 . doi: 10.1016/j.jvolgeores.2016.12.007

Patrick M, Orr T, Fisher G, et al (2016) Thermal mapping of a pāhoehoe lava flow, Kīlauea Volcano. J Volcanol Geotherm Res. doi: 10.1016/j.jvolgeores.2016.12.007

Peterson DW, Holcomb RT, Tilling RI, Christiansen RL (1994) Development of lava tubes in the light of observations at Mauna Ulu, Kīlauea Volcano, Hawaii. Bull Volcanol 56:343–360 . doi: 10.1007/BF00326461

Poland MP, Orr TR, Kauahikaua JP, et al (2016) The 2014-2015 Pāhoa lava flow crisis at Kīlauea Volcano, Hawai'i: Disaster avoided and lessons learned. GSA TODAY | FEBRUARY 2016 GSA TODAY | www.geosociety.org/gsatoday. doi: 10.1130/GSATG262A.1.4

Rossi MJ, Gudmundsson A (1996) The morphology and formation of flow-lobe tumuli on Icelandic shield volcanoes. J Volcanol Geotherm Res 72:291–308 . doi: 10.1016/0377-0273(96)00014-5

Self S, Keszthelyi L, Thordarson T (1998) the Importance of Pāhoehoe. Annu Rev Earth Planet

Sci 26:81–110 . doi: 10.1146/annurev.earth.26.1.81

Turner NR, Perroy RL, Hon K (2017) Lava flow hazard prediction and monitoring with UAS: a case study from the 2014–2015 Pāhoa lava flow crisis, Hawai‘i. J Appl Volcanol 6:17 . doi: 10.1186/s13617-017-0068-3

Walker GPL (1991) Structure, and origin injection of lava under surface crust, of tumuli, “lava rises”, “lava-rse pits”, and “lava-inflation” in Hawaii. Bull Volcanol 53:546–558

Wendel J (2017) Thirteen innovative ways humans use drones. Eos (Washington DC) 98: . doi: https://doi.org/10.1029/2017EO084489

Westoby MJ, Brasington J, Glasser NF, et al (2012) ‘Structure- from- Motion’ photogrammetry: A low- cost, effective tool for geoscience applications. Geomorphology 179:300–314 . doi: 10.1016/j.geomorph.2012.08.021